ImaSim, a Simulation Software Package for the Teaching of Medical X-Ray Imaging

Guillaume Landry

Medical Physics Unit
McGill University
Montréal, Québec, Canada
June 2009

A thesis submitted to the Faculty of Graduate Studies and Research in partial fulfillment of the requirements of the degree Master of Science

ABSTRACT

The goal of this project is to enhance the teaching and the self study of diagnostic and radiotherapy x-ray imaging by creating an interactive educational software package, *ImaSim*, based on a simulation environment. Various imaging modalities found in a radiology or radiation oncology department have been included. *ImaSim* aims at faithfully reproducing the physics behind these modalities while keeping the operation simple and straightforward. Photons simulated fall into the energy range encompassing radiology and radiation oncology. The user can interactively vary many parameters related to image formation. *ImaSim* enables a user to quickly demonstrate and study principles associated with the creation of a radiological image in a classroom or in a self-learning setting. Many imaging phenomena can be studied with the aid of *ImaSim*. This work, by rendering accurate image creation easily accessible, has the potential to enhance textbook based teaching and heighten student interest in medical photon imaging.

RÉSUMÉ

L'objectif de ce projet consiste en l'amélioration de l'enseignement de l'imagerie médicale par la création d'un logiciel interactif, *ImaSim*, basé sur un environnement de simulation. La plupart des modalités d'imagerie médicale propres à un département de radiologie ou radio oncologie se retrouvent dans *ImaSim*. *ImaSim* vise à préserver une utilisation simple tout en modélisant adéquatement les aspects physiques associés aux modalités d'imagerie. Les photons générés tombent dans la gamme d'énergie propre à la radiologie et à la radio oncologie. Plusieurs paramètres liés à la formation d'images peuvent être variés interactivement par l'utilisateur. *ImaSim* permet donc d'étudier les principes associés à la création d'une image radiologique. Plusieurs phénomènes peuvent êtres étudiés à l'aide d'*ImaSim*. Ce projet a le potentiel de complémenter l'enseignement traditionnel de l'imagerie médicale.

ACKNOWLEDGEMENTS

I would like to thank my supervisors, Dr. Frank Verhaegen and Dr. François DeBlois, for their initiative, support, guidance and encouragements. This project would not have been possible without their knowledge and expertise.

Special thanks to Dr. Magdalena Bazalova, whose knowledge of computed tomography and Monte Carlo techniques proved to be invaluable. I would also like to thank the students and staff of the Medical Physics Unit at McGill University for their support and many helpful discussions.

I wish to thank NSERC and the Government of New Brunswick for providing me with the financial means to pursue studies at the master's level.

Finally, I would like to thank Céline for supporting me throughout my Montréal studies.

TABLE OF CONTENTS

LIST OF TABLES

LIST OF FIGURES

CHAPTER 1: INTRODUCTION

1.1 Brief Historical Introduction to Medical X-Ray Imaging

Medical x-ray imaging was born in 1895, following Roentgen's discovery of x-rays and their ability to penetrate human tissues. Using a piece of film as a detector, Roentgen captured the first radiographic image[1]. X-rays have been used in medicine ever since. Although radiographs are still widely used in hospitals today, some new x-ray based imaging techniques have been developed. 1972 saw the introduction, by Hounsfield, of the first x-ray computed tomography (CT) machine[2], capable of imaging sections of a body. These scanners have been constantly perfected, enabling us to image whole sections of the human body in three dimensions. A recent advancement consists of using a relatively large rectangular detector array instead of the standard ring array. These scanners, called cone beam computed tomography (CBCT) machines[3], can acquire data over larger areas, speeding up scan times. The purpose of x-ray imaging has also evolved, being purely diagnostic in its beginnings, we now see x-ray images taken with the treatment beams of linear accelerators, their purpose to verify patient alignment and motion in radiotherapy[4].

1.2 The Teaching of Medical X-Ray Imaging

Given the importance of medical x-ray imaging for diagnostic or other purposes in medicine, there is a necessity to teach a number of healthcare professionals some aspect or another of this science. Medical physicists, radiologists, radiation oncologists, technologists, engineers and many more all need some degree of formation in the field. For the purpose of teaching, any imaging modality briefly introduced in Section 1.1 can be deconstructed into four basic components as shown in Fig. 1.

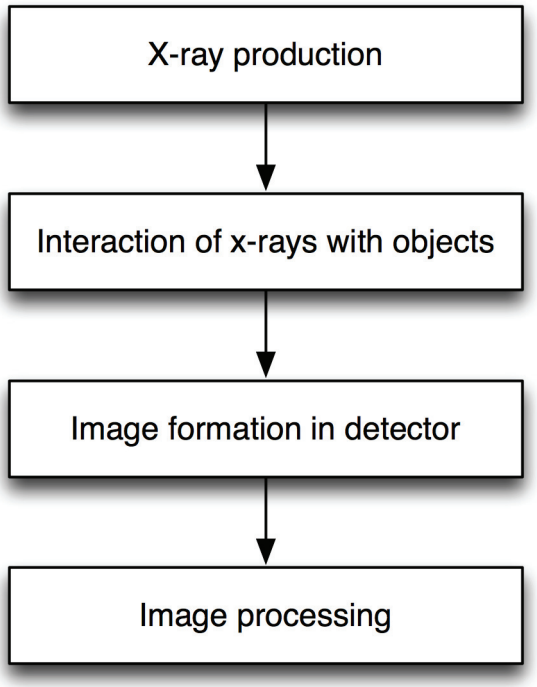

Figure 1: Four basic components of any imaging modality.

X-ray production covers all the parameters and principles related to the production of x-ray beams. *Interactions of x-rays with objects* consists of the physics governing the way x-rays and matter interact. *Image formation in detector* is how x-rays are captured by detector elements and translated into images. Finally, *image processing* is the sum of all image analysis methods and tools. For the medical physicist or engineer, the physics and mathematics of each of these components must be fully understood, while a more qualitative understanding of cause and effect may be sufficient for other professionals.

1.3 Motivation for the Creation of a Simulation Software Package

At any level, a hands on approach coupled to classroom teaching can be beneficial to the understanding of the imaging process. Unfortunately for most students, imaging equipment is generally monopolized by patient care, restraining the amount of time students can spend experimenting with principles learned in the classroom and their effects on image quality. Furthermore, it is often difficult to vary imaging parameters in a clinical setting, since the equipment

has been designed for some specific purpose. Therefore, there is a clear need for a software package based on a simulation environment capable of producing virtual medical x-ray images. Such a software package would serve as a powerful educational tool for medical x-ray imaging.

1.4 Thesis Objectives

The objective of this thesis is to elaborate a software package containing a simulation environment for medical x-ray imaging, named *ImaSim*, to be used as teaching tool. *ImaSim* should be highly interactive and its utilisation should be intuitive and simple, thanks to a graphical user interface (GUI) both simple and visually appealing. *ImaSim* should also cover the following x-ray based imaging modalities:

- Planar kV imaging
- Planar MV imaging
- CT imaging
- CBCT imaging

ImaSim also needs to be useable both in a classroom setting by an educator for virtual demonstrations of imaging phenomena, as well as in a self learning setting by a student for virtual experimentation purposes. In both cases, the user must be able to demonstrate or study the effects of varying imaging parameters on the quality of the final medical image. These parameters fall into five categories, corresponding to the five steps a user needs to go through to obtain a virtual image. These five categories of parameters are:

1. X-ray production
2. Object creation
3. Geometrical setup
4. Detector selection
5. Modality dependant image processing

REFERENCES

[1] M. Hoheisel, "Review of medical imaging with emphasis on X-ray detectors," Nuclear Instruments and Methods in Physics Research A **563**, 215-224 (2006).

[2] S. Webb, *The Physics of Medical Imaging*. (Institute of Physics Publishing, Bristol, 1988).

[3] T. M. Buzug, *Computed Tomography*. (Springer, Berlin, 2008).

[4] J. V. Dyk, "The Modern Technology of Radiation Oncology," (Medical Physics Publishing, Madison, 1998).

CHAPTER 2: THEORY

2.1 Principles of Imaging

2.1.1 X-rays

The basis of medical x-ray imaging is, of course, the x-ray. X-rays in medicine are photons of energies either in the keV or few MeV range. It is generally understood that to be considered x-rays, photons need to originate from electron transitions or bremsstrahlung.

2.1.2 The x-ray image

At the core of any medical x-ray image, whatever the modality, is the interaction of x-rays and an x-ray detector. X-rays emanating from a source and going through an object will either be absorbed, scattered or traverse it unaffected. The scattered x-rays contain little information on the object being imaged and will generally degrade image quality if they reach the x-ray detector. It is the unaffected x-rays reaching the detector, called primary photons, which yield the information on the object being imaged. Their number is correlated to their probability of interaction with the object in question. This probability is in turn related to the physical properties of the sum of materials traversed by the photons. X-ray images are thus based on two-dimensional projections, projections of the physical properties of three-dimensional objects along the path of x-rays[1]. Depending on the imaging modality, these projections can be final images, or undergo further processing.

2.1.3 X-ray production

2.1.3.1 Kilovoltage x-rays

Conventional x-rays are in the keV range. They are generally produced using x-ray tubes where electrons are accelerated under vacuum from a cathode to a tungsten anode. The potential difference used to accelerate electrons is usually between a few tens of kV to 300 kV. The cathode is normaly a heated filament, which releases electrons via thermionic emission. Tungsten is generally

chosen as anode material since it has a high atomic number, which gives it a better x-ray yield. It also has a high melting point; the beam of electrons hitting the anode creates large amounts of heat. For this reason, the beam cannot be infinitesimal in size or it would burn a hole in the tungsten. Furthermore, the anode is angled to provide a large area for electrons to hit it while keeping a reasonable effective focal spot size, as shown in Fig. 2. A smaller effective focal spot size reduces geometrical blurring.

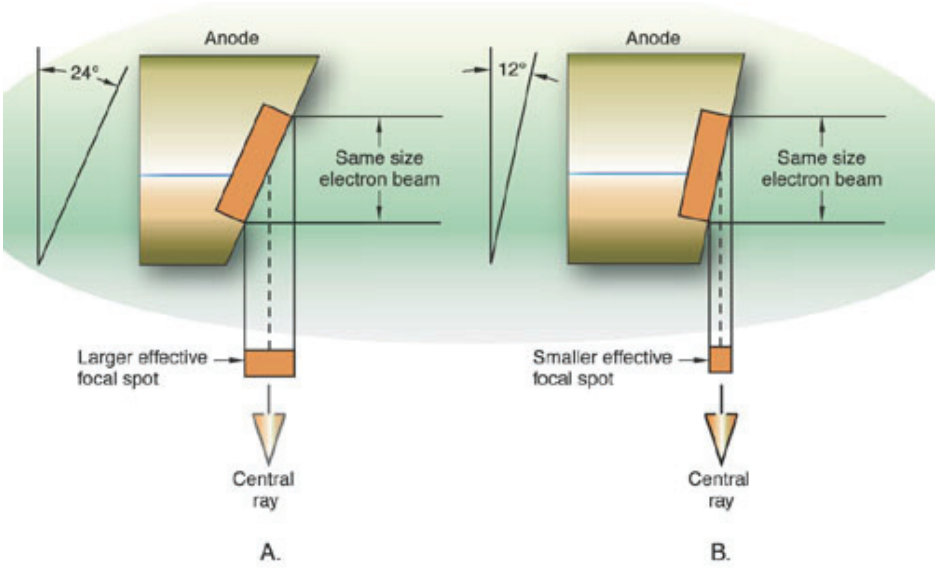

Figure 2: Effect of an angled anode. The effective focal spot size is smaller than the electron beam size. Furthermore, the area of the anode exposed to electrons is also larger than the size of the electron beam. Increasing the anode angle in (A) increases the field size and the effective focal spot size compared to (B). Courtesy *whs.wsd.wednet.edu*.

Electrons striking the tungsten target will penetrate it and lose their energy. About 1% of this energy results in usable x-rays, the rest is dissipated as heat. There are two processes leading to the production of x-rays: bremsstrahlung and characteristic radiation.

Bremsstrahlung involves interactions between the electrons and tungsten nuclei. When passing near a nucleus, the electron is deflected by the Coulomb interaction between itself and the nucleus. This deflection is accompanied by a kinetic energy loss that is translated into the emission of x-rays. An electron will

normally undergo many of these interactions, producing photons of various energies at various depths in the anode. The maximum energy loss possible is in the case of a head on collision with a nucleus, where a photon having the electron's entire kinetic energy is created. A continuous spectrum of x-rays is thus created by bremsstrahlung. This spectrum has more low energy photons than high energy photons.

Characteristic radiation is characterized by the interaction of an electron with a bound electron. The bound electron, which is usually in the inner orbits of the atom, is ejected. A higher orbit electron will then take its place and, according to a certain probability, will emit a single x-ray in the process. Since the energies of the emitted x-rays will be characteristic of the atomic structure of the target element, they are called characteristic x-rays.

In both these cases, the x-ray spectrum coming out of the tube is not the same as the one being directly emitted by the electrons and atoms. Since some x-rays are produced within a certain depth in the target, they undergo interactions with the target material, which then acts as an intrinsic filter. More filtration is usually required at the exit of the tube to obtain an adequate spectrum. An example of such a spectrum is found in Fig. 3.

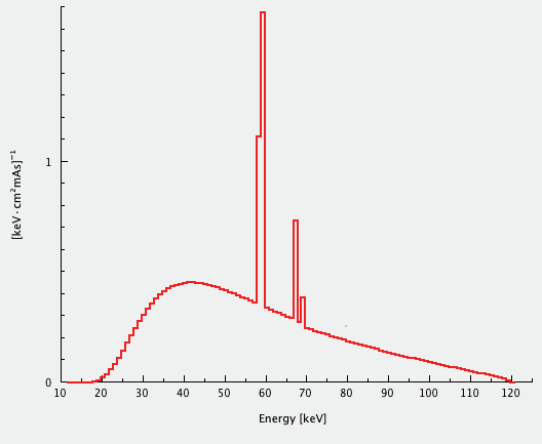

Figure 3: Typical x-ray spectrum at exit of tube. Visible are the bremsstrahlung spectrum along with the characteristic peaks caused by tungsten's characteristic x-rays. (Image produced with *SpekCalc* [2])

2.1.3.2 Megavoltage x-rays

The modern treatment device in radiotherapy is the linear accelerator (LINAC). LINACs provide photon beams in the MeV range for treatment. The principle behind the creation of these photon beams is the same as in kV beams: high energy electrons striking a target of some material. The main difference with the LINAC is the method for accelerating the electrons. A radio frequency waveguide composed of a series of resonating cavities is used to obtain electrons having kinetic energies in the MeV range. These electrons then strike a transmission target thick enough to stop all electrons and produce x-rays via bremsstrahlung. Characteristic radiation is negligible at this energy range, since the largest binding energy for an atomic electron is around 100 keV.

2.1.4 X-ray interactions with matter

X-ray photons interact with matter by one of the following processes:

- Coherent scattering
- Photoelectric effect
- Compton scattering
- Pair production

X-rays produced from x-ray tubes, with energies usually below 300 keV, do not undergo pair production interactions. This interaction is only relevant for photons in the megavoltage range, with energies larger than 1.022 MeV.

2.1.4.1 X-ray beam attenuation

A narrow beam of x-rays passing through a given uniform material will be attenuated. Assuming the beam contains x-rays of various energies, the number $N_E(x)$ of photons of energy E at depth x in the material of density ρ is given by:

$$N_E(x) = N_E(0)e^{-\frac{\mu}{\rho}\rho x} \qquad [2.1]$$

where $N_E(0)$ is the original number of photons of energy E before attenuation and μ/ρ is the total mass attenuation coefficient of the material at that energy. The total mass attenuation coefficient contains contributions from the four x-ray interaction types:

$$\frac{\mu}{\rho} = \frac{\tau}{\rho} + \frac{\sigma_R}{\rho} + \frac{\sigma}{\rho} + \frac{\kappa}{\rho} \qquad [2.2]$$

where τ/ρ is the mass attenuation coefficient from the photoelectric effect, σ_R/ρ from coherent scattering, σ/ρ from Compton scattering and κ/ρ is from pair production.

The attenuation of an x-ray beam is thus material and energy dependent. This is shown in Fig. 4 and Fig. 5 where the mass attenuation coefficients of low and high Z elements or compounds are found. Photons removed from the beam are either absorbed or scattered, depending on the type of interaction they undergo.

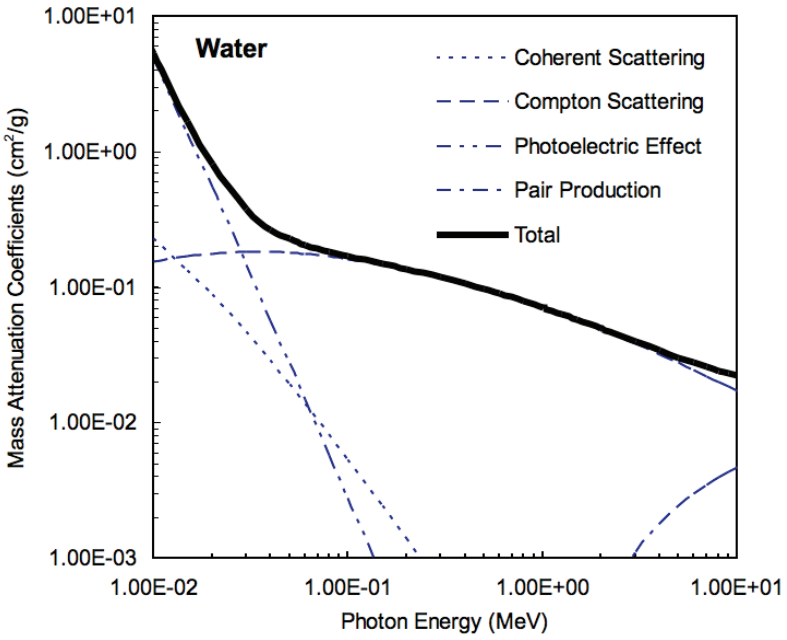

Figure 4: The various mass attenuation coefficients of water (effective $Z \approx 7$) and their sum over the energy range used in diagnostic or portal imaging. Notice that pair production is negligible in this energy range. (Compiled with data from the web database XCOM)

2.1.4.2 Coherent scattering

In a coherent scattering interaction, an x-ray's direction is modified but not its energy. Coherent scattering covers two interactions: Thompson scattering and Rayleigh scattering. The first is considered to be an interaction between a low energy x-ray and a single electron, while the second consists of the interaction of an x-ray and all the electrons of an atom[3]. Coherent scattering is never the dominant interaction, whatever the energy range or atomic number.

Although scatter affects image quality negatively, coherent scattering is not too problematic in imaging since the other interaction types usually overshadow it. Coherent scattering can be important in mammography where energies are much lower.

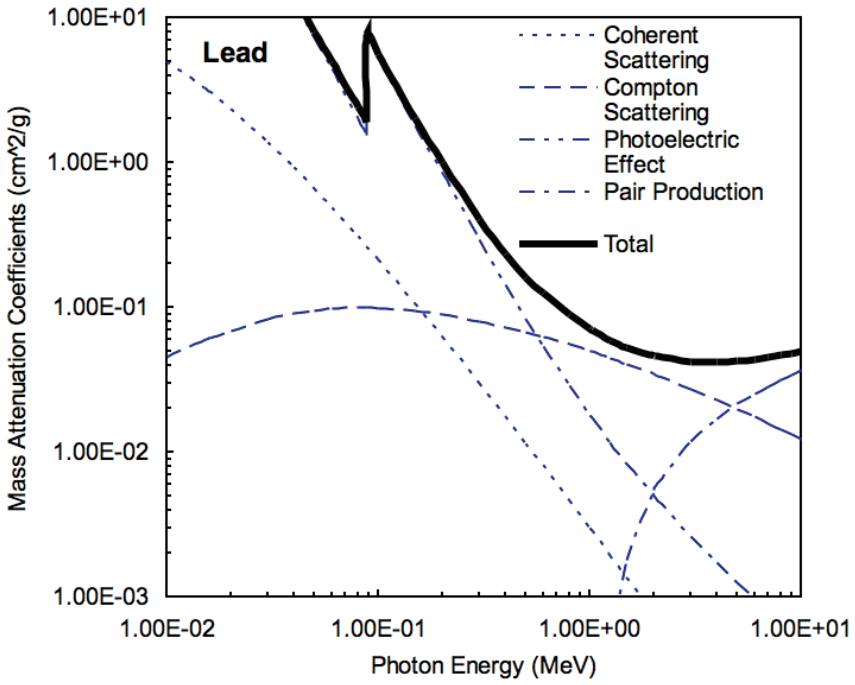

Figure 5: The various mass attenuation coefficients of lead ($Z = 82$) and their sum over the energy range used in diagnostic or portal imaging. (Compiled with data from the web database XCOM)

2.1.4.3 Photoelectric effect

A photoelectric interaction consists of an x-ray ejecting an inner shell electron from an atom. The photon's energy is completely expended in the process and the photon disappears. The ejected electron, called photoelectron, receives this energy and uses it to overcome its binding energy, the rest translating to kinetic energy. A photon having energy smaller than the electron's binding energy will not undergo photoelectric interaction with this electron. Furthermore, the likelihood of occurrence increases when the photon's energy is close to the electron's binding energy. This yields the E^{-3} dependence of the photoelectric effect's mass attenuation coefficient.

The probability of a photoelectric interaction is also higher for inner shell electrons, which are tightly bound. Provided a sufficient photon energy, the photoelectric effect will thus favour the K shell. This also leads to the Z^3 dependence of the photoelectric effect's mass attenuation coefficient, where Z is the atomic number, since higher Z elements have larger binding energies.

The photoelectric effect usually dominates in the low keV range. Its dominance is extended with increasing atomic number, but never in the MeV range.

The photoelectric effect is beneficial for image quality since it does not produce scattered photons: a photoelectric interaction ends the photon's path. This can have a detrimental effect on the patient's health since most of the photon's energy will be deposited in him. The Z^3 dependence also provides good contrast between different tissues having different atomic numbers.

2.1.4.4 Compton scattering

Compton scattering consists of an interaction between a photon and a loosely bound electron. In such an interaction, the electron is ejected from the atom with a certain kinetic energy. The incoming photon is absorbed and a scattered photon is produced, having a lower energy. By loosely bound electron, one generally means an electron whose binding energy is much smaller than the incident photon's energy.

The mass attenuation coefficient for Compton scattering is essentially independent of Z and decreases with photon energy[4] E.

The escaping photons can be scattered over 360 degrees, although the proportion of forward scattered photons is larger and increases with the photon energy. In the keV range, photons that are scattered forward tend to have energies similar to the incoming photon's energy. This causes a problem for imaging since it becomes difficult to differentiate between primary photons and scattered ones since they have similar directions and energies.

2.1.4.5 Pair production

Pair production is an interaction between a photon and the Coulomb field of a nucleus. It consists of the disappearance of the photon and the creation of an electron-positron pair. In order to undergo a pair production interaction, a photon needs to have a minimal energy of 1.022 MeV. Its probability increases rapidly with photon energy and its mass attenuation coefficient increases linearly with atomic number. Given the high threshold energy, this mode of interaction is irrelevant for imaging in the keV range but can be significant for megavoltage imaging.

2.1.4.6 Beam hardening

The variation of attenuation with energy has an important effect on an x-ray spectrum. This effect is generally associated with kV beams, where the variation of attenuation with energy is drastic due to the rapid decrease of the photo electric effect's mass attenuation coefficient. The fact that low energy photons are preferentially removed from an x-ray beam traversing a medium will change its spectrum and increase its mean energy with penetration depth. This mean energy increase means the beam is less likely to be attenuated, or is hardened. This is shown in Fig. 6.

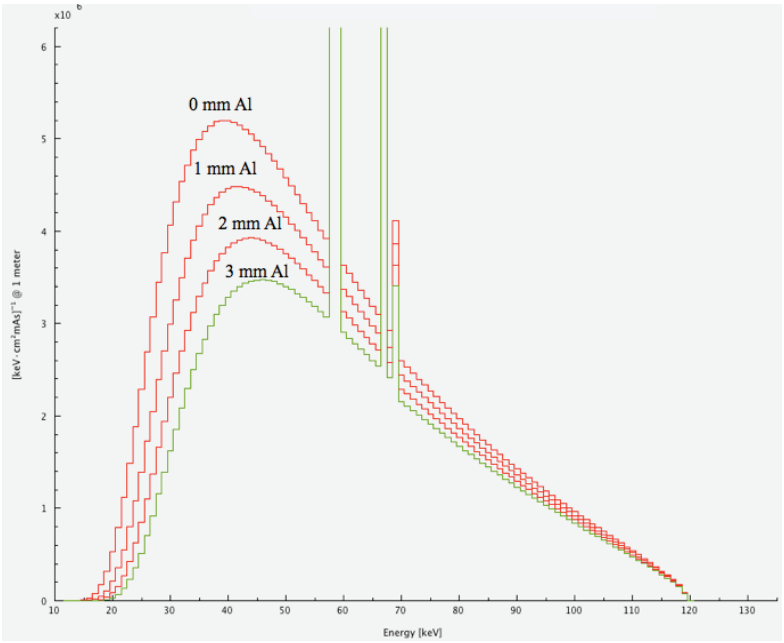

Figure 6: Four 120 kVp x-ray spectra with 0, 1, 2 and 3 mm Al in the beam. The beam's mean energy increases with added filtration, hence the term beam hardening.

2.1.5 X-ray detection

X-ray detection is based on the absorption, by some material, of the photon's energy. Following this energy absorption, various processes are employed, depending on the type of detector, to convert the deposited energy into an image. An ideal detector should not decrease the signal to noise ratio present in the incident photon fluence. It should thus totally absorb the energy of the incident x-rays. The efficiency of the conversion of the deposited x-ray energy to the image must also be high. While trying to fulfill these requirements, it is important to preserve an adequate spatial resolution.

2.1.5.1 Kilovoltage planar imaging

The purpose of a kilovoltage planar imaging detector is to cover x-ray detection up to 150 keV. Although x-ray tubes can reach accelerating potentials of 300 kV, they are not used for imaging purposes.

A. Film screen

Up until the 1980s, the film screen combination was the most widely used detector for kilovoltage radiographies. It consists of a two sided film sandwiched between two phosphor screens. The phosphor screens absorb the x-ray energy and convert it to visible light. This light, when interacting with the active layers of the film, which consist of silver halide grains in gelatine, modifies the grains. Upon development of the film, the modified grains become silver and darken the film. A typical phosphor material is Gd_2O_2S:Tb (Gadox), which emits green light. The resolution of phosphor screens is inversely proportional to their thickness, since the light emission is isotropic.

B. Computed radiography

Computed radiography (CR), which appeared in the 1980s, brought radiographs into the digital age. It eliminated the need for film developers and dark rooms. CR is based on a storage phosphor which can be read out with a laser. X-rays interacting with the phosphor leave some of its electrons in an exited state. By illuminating the phosphor with a laser, these electrons fall back to their initial state, emitting light by fluorescence. By measuring this light, a digital radiographic image is created. A typical storage phosphor material is $BaFBr:Eu^{3+}$. CR cassettes have a much larger exposure range than screen film technology but still require bulky read out scanners.

C. All digital imaging

Flat panel detector technology provides an all digital solution to diagnostic imaging. These panels provide a digital image following exposure with no intermediary steps. The underlying technology is based on a large amorphous silicon thin film, forming an array of transistors responsible for the read out of each pixel element of the matrix[5] . The signal in each pixel comes either from a scintillator film coupled to a photodiode or from a semiconductor layer. In the latter, electrons-hole pairs are directly created by x-ray interaction and collected downward with an electric field. This provides an excellent resolution. Amorphous

selenium or silicon is usually used as semiconductor. In the case of the scintillator film, CsI:Tl is used. It is grown in a columnar structure which acts as a light guide and enhances resolution[6] .

2.1.5.2 Portal imaging

In portal imaging, detectors must be tuned to the higher x-ray energies encountered, usually around 1-6 MeV.

A. Radiotherapy film systems

Historically, portal images were taken with a film screen setup. The phosphor screens were replaced by thin metal plates, usually copper, which provided electronic build up. The electrons exposed the film. The back plate was used to provide electron backscatter[7] . The cassettes were improved by sandwiching the film between a phosphor screen pair and removing the back plate, while keeping the front metal plate. Portal films require development, which renders the imaging procedure time consuming.

B. Electronic portal imaging devices (EPIDs)

EPIDs are a replacement to the film systems. They provide a digital portal image immediately after exposure. The first generation of EPIDs were either based on a matrix of ionisation chambers or a scintillator coupled with a TV camera.

In the matrix ion chamber setup, a liquid (2,2,4-trimethylpentane) is enclosed between two electrodes. Charges created in the liquid by the radiation are collected by the electrodes.

The TV camera based EPIDs consist of a Gd_2O_2S screen covered with a copper plate. The visible photons are collected by a 45 degree mirror and a TV camera. The video signal is then digitized[8].

More recently, amorphous silicon flat panel technology has been applied to portal imaging. The detectors are similar to the flat panel imagers described in

the kilovoltage imaging section. The main difference is the addition of a metal plate on top of the arrays to provide electronic buildup.

2.1.5.3 CT imaging

In CT imaging, assuming a single slice scanner, x-ray detection is handled by a one dimensional array of detector elements. These detectors are disposed on a ring, which either covers 360 degrees or only the width of the x-ray beam. Each element consists of a scintillation crystal, usually CsI:Tl, coupled to a photodiode. Once again, the technology is similar to the flat panel imager technology described in the kilovoltage imaging section.

2.1.5.4 CBCT imaging

CBCT imaging requires large ($\sim$40 cm $\times$ 40 cm) digital imaging panels tuned to kilovoltage or megavoltage energies. Flat panel digital imagers discussed in the kilovoltage planar imaging and portal imaging sections are usually used as detectors for CBCT application, thus no additional information is required on the subject.

2.2 Imaging Modalities

X-ray imaging can be divided in two categories: diagnostic imaging and radiotherapy verification imaging. In diagnostic imaging, an x-ray tube is used as photon source with maximum accelerating potential around 150 kVp. The purpose is to obtain diagnostic or anatomical information of the patient. Verification imaging can use an x-ray tube or a treatment unit, usually a LINAC, as photon source. The purpose here is the verification of patient alignment and treatment delivery. Imaging modalities can thus be divided into two families, as shown in Table 1.

Imaging Modalities	
X-ray tube based	**LINAC based**
Planar radiography	Portal imaging
CT	Megavoltage CT (MVCT)
kV-CBCT	Megavoltage CBCT (MV-CBCT)

Table 1: Imaging modalities classified by x-ray source

2.2.1 Planar radiography

Planar radiography, or kilovoltage planar imaging, is the most widespread imaging modality. It consists of an x-ray tube coupled to an x-ray detector which can be a film-screen cassette, a CR cassette or a digital flat panel detector. The images produced are two dimensional projection radiographs of the patient. A wide array of parameters come into play when taking a radiograph: tube potential, tube current, exposure time, source to patient and source to detector distances, focal spot size and many more. It is beyond the scope of this thesis to delve into these details. The reader is referred to Christensen's Physics of Diagnostic Radiology by Curry for a complete description[3].

2.2.2 CT

CT imaging is now a mainstay in diagnostic radiology and radiation oncology. The aim of CT imaging is to obtain cross sectional images of the human body. To do so, a CT scanner acquires one dimensional radiographs, or projections, of the patient over 360 degrees. With the aid of computer algorithms, it is possible to reconstruct the internal structure of the patient with this set of projections.

The overview given here will be brief. For a complete description the reader is referred to Computed Tomography by Buzug[9].

2.2.2.1 Geometrical setup and projection acquisition

There has been at least four main generations of CT scanners. Third generation scanners, which are commonplace in many hospitals, will be discussed here. These CT scanners consist of an x-ray tube that can rotate over 360 degrees around an isocenter. The beam is collimated to a fan shaped slice. Coupled to this x-ray tube is a curved detector array whose radius of curvature corresponds to the source to detector distance, as shown in Fig. 7. Each detector element is usually equipped with its own collimator to reduce the effects of scattered x-rays.

The x-ray tube and detector rotate around the patient and acquire a number of one dimensional projections of an axial slice of the patient. These projections are then sent to a computer which handles the reconstruction of the slice.

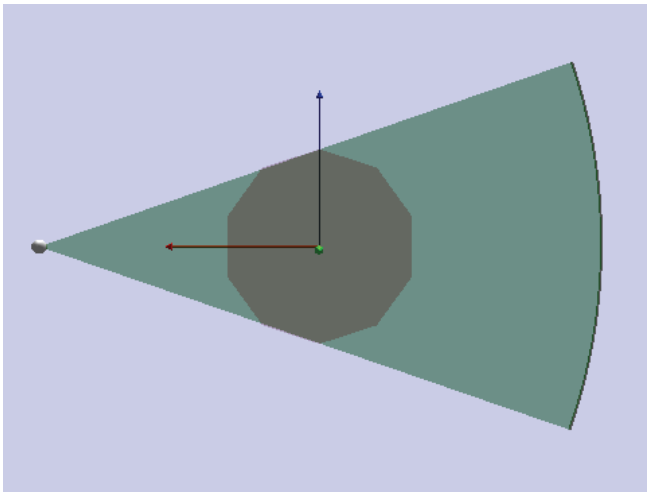

Figure 7: Third generation CT scanner source-detector setup. The source-detector setup rotates around the green axis, visible as a dot here. This rotation axis is parallel to the superior/inferior direction.

2.2.2.2 Reconstruction method

Although most clinical scanners use a fan beam setup, it is simpler to discuss image reconstruction by considering a parallel beam setup impinging on a flat detector array. Furthermore, we will assume a monoenergetic source. In this setup the x-ray tube would be collimated to a pencil beam. For each tube

position around the patient the tube itself is translated so each detector element is exposed. For detector element i and tube angle θ the projection data is:

$$p_\theta(t_i) = -\ln\left(\frac{N(0)e^{-\int_0^s \frac{\mu}{\rho}(x)\rho(x)dx}}{N(0)}\right) = \int_0^s \frac{\mu}{\rho}(x)\rho(x)\,dx = \int_0^s \mu(x)dx \qquad [2.3]$$

where t_i is the ith detector element's position, $N(0)$ is the initial number of photons, x denotes the position along the x-ray path and s is the source-detector distance.

A. Backprojection

The standard reconstruction method is the filtered backprojection. The procedure consists of filtering the projections, which will be discussed later, and backprojecting them onto an image matrix. For a given pixel and tube position, we interpolate the value of equation 2.3 from the projection data for the ray passing at the center of the pixel. This value is then added to the pixel. This is done for every pixel and tube position. The backprojection can be seen as smearing the filtered projection data of every tube position over the image matrix.

Doing this without modifying the data will result in an unusable image. The backprojection will yield an image corresponding to the convolution of the original image with a $1/r$ blurring kernel, r being the radial distance from the center of the image. This is the reason why the data needs to be filtered prior to backprojection

B. Filtering

The standard way to handle the modification of the projection data is to apply frequency filters in Fourier space. The Fourier transform of $p_\theta(t)$ is $P_\theta(k_t)$ where k_t is the spatial frequency. An analytical treatment shows that in the absence of noise, the backprojection yields the correct values if a ramp filter is applied to the projections. The modified projections $p'_\theta(t)$ are thus given by:

$$p'_\theta(t) = \mathcal{F}^{-1}\left\{P_\theta(k_t)\cdot|k_t|\right\} \quad [2.4]$$

where $\mathcal{F}^{-1}$ denotes the inverse Fourier transform. The resulting image will be a two dimensional map μ_{ij} of the linear attenuation coefficients of the cross section of the body.

2.2.2.3 Hounsfield values

The μ_{ij} values are usually rescaled to Hounsfield units (HU):

$$HU_{ij} = \frac{\mu_{ij} - \mu_{\text{water}}}{\mu_{\text{water}}} \cdot 1000 \quad [2.5]$$

where μ_{water} is the attenuation coefficient of water for the beam energy used.

2.2.3 CBCT

CBCT imaging has been growing rapidly in recent years thanks to advances in flat panel technology. Since fast large area detectors are now available, it is possible to acquire series of two dimensional projections around the human body. With adequate reconstruction algorithms, it is possible to reconstruct a three dimensional volume from a single tube-detector revolution around the patient.

2.2.3.1 Geometrical setup and projection acquisition

Once again, the setup consists of an x-ray tube and detector arrangement capable of rotating over 360 degrees. The beam is now collimated to cover a square and flat detector array. It is important to note the absence of collimation for each detector element, which increases the effect of scattered radiation.

The overview given here will be brief. For a complete description the reader is again referred to Computed Tomography by Buzug[9].

2.2.3.2 Reconstruction method

A reconstruction method for CBCT is the FDK algorithm[10]. The algorithm is based on the filtered backprojection presented in Section 2.2.2. The data

consists of two dimensional projections $p_\theta\left(x_i, y_j\right)$ where x_i is the position of i th detector element in the direction perpendicular to the axis of rotation (rows) and y_j is the j th detector element in the direction parallel to the axis of rotation (columns).

A. Weighting and filtering

To simplify calculations, it is assumed that the detector is at the axis of rotation. A simple scaling of the detector element positions is thus performed:

$$a = x_i \cdot \frac{FCD}{FDD}, b = y_j \cdot \frac{FCD}{FDD}. \qquad [2.6]$$

FCD is the source to center distance, FDD is the source to detector distance and ab are the new coordinates. The subscripts i and j have been dropped to simplify the notation. Prior to the filtering, the data is weighted in the following manner:

$$p'_\theta(a,b) = p_\theta(a,b) \cdot \frac{FCD}{\sqrt{FCD^2 + a^2 + b^2}}. \qquad [2.7]$$

The data for each detector row is then filtered the same way a one dimensional projection is filtered in CT. The data in the detector row is Fourier transformed and a ramp filter is applied. The inverse transform yields the filtered data for each detector row.

B. Backprojection

Any value $f(x,y,z)$ at a point (x,y,z) in the volume covered by the x-ray beam can be reconstructed from the dataset. The coordinates are not to be confused with (x_i, y_j) which denote detector elements. The x axis is normal to the sagittal plane, the y axis is normal to the coronal plane and the z axis is normal to the axial plane. The reconstructed values are given by the following equations:

$$f(x,y,z) = \int_0^{2\pi} \frac{FCD^2}{U(x,y,\theta)^2} p'_\theta\left(a(x,y,z,\theta), b\left(x,y,z,\theta\right)\right) d\theta \qquad [2.8]$$

$$U = FCD - x\sin\theta + y\cos\theta \quad [2.9]$$

$$a = FCD\frac{x\cos\theta + y\sin\theta}{FCD - x\sin\theta + y\cos\theta} \quad [2.10]$$

$$b = z\frac{FCD}{FCD - x\sin\theta + y\cos\theta}. \quad [2.11]$$

To use these equations, it is important to correctly measure the rotation angle. With the b axis pointing towards the reader, the angle of rotation increases clockwise.

2.2.4 Portal imaging

Portal imaging, or megavoltage planar imaging, is used in radiotherapy. It consists of the acquisition of planar images with the x-ray beam of a treatment LINAC coupled to an EPID. At megavoltage energies, the dominant photon interaction is Compton scattering. Since the mass attenuation coefficient for Compton scattering is independent of atomic number, contrast in the portal image is mainly obtained by density differences. Since most soft tissues have similar densities, portal imaging principally shows bony anatomy. Portal images are taken before radiotherapy and used to position the patient, based on the bony anatomy. The reader is referred to The Modern Technology of Radiation Oncology edited by Dyk for a review of the subject[8].

2.2.5 MVCT

As the name implies, MVCT is a variant of CT where an MV source is used instead of a kV one. MVCTs can be acquired with a helical tomotherapy unit (TomoTherapy, Inc., Madison, WI) for example. The mathematical treatment is identical to kV CT.

2.2.6 MV-CBCT

Similarly, MV-CBCT is a variant of CBCT. A MV-CBCT scan is usually taken with a treatment LINAC equipped with an EPID, generally amorphous silicon based. The reconstruction algorithm is the same as in CBCT.

REFERENCES

[1] S. Webb, *The Physics of Medical Imaging*. (Institute of Physics Publishing, Bristol, 1988).

[2] G. Poludniowski, G. Landry, F. DeBlois and F. Verhaegen, "SpekCalc X-ray Spectrum Generator Programme," (The Institute of Cancer Research, 2008).

[3] T. S. Curry, J. E. Dowdey and R. C. Murry, *Christensen's Physics of Diagnostic Radiology*, 4th ed. (Lea & Febiger, Philadelphia, 1990).

[4] E. B. Podgorsak, *Radiation Physics for Medical Physicists*. (Springer, Berlin, 2006).

[5] M. Hoheisel, "Review of medical imaging with emphasis on X-ray detectors," Nuclear Instruments and Methods in Physics Research A **563**, 215-224 (2006).

[6] J. P. Moy, "Recent developments in X-ray imaging detectors," Nuclear Instruments and Methods in Physics Research A **442**, 26-37 (2000).

[7] L. E. Antonuk, "Electronic portal imaging devices: a review and historical perspective of contemporary technologies and research," Physics in Medecine and Biology **47**, R31-R65 (2002).

[8] J. V. Dyk, "The Modern Technology of Radiation Oncology," (Medical Physics Publishing, Madison, 1998).

[9] T. M. Buzug, *Computed Tomography*. (Springer, Berlin, 2008).

[10] L. A. Feldkamp, L. C. Davis and J. W. Kress, "Practical cone-beam algorithm," Journal of the Optical Society of America A **1**, 612-619 (1984).

CHAPTER 3: MATERIALS AND METHODS

3.1 Development Platform

REALbasic (REAL Software, Inc., Austin, Texas) has been chosen to develop *ImaSim*. It is a high-level visual programming environment. It provides a GUI development environment suited to the needs of a teaching software package. The ability to build three dimensional environments as well as aesthetically pleasing GUIs guided the choice. Furthermore, applications designed with REALbasic can be compiled for the three major operating systems: Windows, Mac and Linux.

3.2 Simulation Exactness and Calculation Speeds

Ideally, a simulation would take into account every known aspect of the modeled phenomenon. This would yield the best results possible. When designing teaching software, another constraint comes into play. It is necessary to have low calculation times, especially for classroom usage. The educator needs to be able to show results at the click of a button, otherwise student interest might fade. These two opposing principles must thus be balanced to yield an adequate tool.

3.3 Modular Approach

ImaSim has been developed with a modular approach. To simplify the development as well as the learning experience, the imaging chain has been broken down into a series of modules. They are the following:

- Source creation
- Object creation
- Geometrical setup
- Detector modelling
- Photon interaction
- Data processing
- Image tools

While going through a simulation, the user must choose parameters related to each module in an ordered fashion. For example, *photon interaction* cannot take place before *source creation*. The GUI presents these modules with a logical and easy to grasp flow. The physics and mathematics involved with each module is modelled according to the requirements of calculation speeds and simulation accuracy. The following sections will describe each of these modules and the parameters they manage.

3.4 Source Creation

3.4.1 Kilovoltage sources

In *ImaSim,* kilovoltage source creation is handled by *SpekCalc*, a kilovoltage spectrum creation tool which is based on a verified model. With *SpekCalc*, accelerating potentials of up to 300 kV with a tungsten anode can be modelled. Spectra in *SpekCalc* are created in a two step process. The first step consists of electron transport in the tungsten anode[1] while the second step is photon spectrum calculation[2].

Electron transport is modeled by a joint frequency density $f(u,x)$ which is the number density of electrons reaching a depth x with fraction of the initial kinetic energy u. The model decomposes the joint frequency density as follows:

$$f(u,x) = \eta_{\mathrm{F}}(x) P_{\mathrm{F}}(u \mid x) + \eta_{\mathrm{M}}(x) P_{\mathrm{M}}(u \mid x) \qquad [3.1]$$

where $\eta(x)$ is a planar survival frequency representing the frequency at which an electron reaches depth x and $P(x \mid u)$ is the probability, referred to as conditional probability function (CPF), that such an electron has energy fraction u. The subscripts F and M represent the first and multiple pass components of the electron fluence. This treatment is necessary since electrons in a target are scattered multiple times and will go through a plane more than once.

The planar survival frequencies are modeled with equations verified by Monte Carlo simulations while the CPFs are taken directly from a 100 keV Monte Carlo simulation and scaled accordingly to the accelerating potential under investigation. This model provides an accurate representation of electron

transport in tungsten anodes and can be used for incident energies of up to 300 keV.

The number of photons $N_{\text{emit}}(h\nu)dh\nu$ created in the energy range $h\nu$ to $h\nu + dh\nu$ is given by the following double sum over all depths x and energy fractions u:

$$N_{\text{emit}}(h\nu)dh\nu = d_x n\left(\int_0^{\infty}\int_{h\nu/T_0}^{1}\frac{\Phi\left(h\nu, T_{\text{i}}(u)\right)}{T_{\text{i}}(u)}f(u,x)\,du\,dx\right)dh\nu \qquad [3.2]$$

where n is the number density of target atoms, d_x is a path length correction taking the value 2.00, $T_{\text{i}}(u)$ is the kinetic energy of an electron with energy fraction u and $\Phi\left(h\nu, T_{\text{i}}(u)\right)$ is a differential cross section for photon emission in the range $h\nu$ to $h\nu + dh\nu$ from such an electron. The cross section used in *SpekCalc* is a semi relativistic approximation of the Bethe-Heitler bremsstrahlung cross section with Elwert correction factor f_{E}:

$$\Phi\left(h\nu, T_{\text{i}}\right) = Z^2 {r_0}^2 \alpha \frac{2}{3}\frac{T_{\text{i}}}{h\nu}\frac{1}{p_{\text{i}}^2 c^2}\left[4E_{\text{i}}E_{\text{i}}L - 7\,p_{\text{i}}cp_{\text{f}}c\right]f_{\text{E}}, \qquad [3.3]$$

$$L = 2\ln\left(\frac{E_{\text{i}}E_{\text{f}} + p_{\text{i}}cp_{\text{f}}c - m^2c^4}{mc^2 h\nu}\right), \qquad [3.4]$$

$$f_{\text{E}} = \frac{p_{\text{i}}}{p_{\text{f}}}. \qquad [3.5]$$

In the above equations the subscript i refers to the electron before the emission of a bremsstrahlung photon of energy $h\nu$ and the subscript f refers to the electron following the emission. E represents the relativistic energy, p the momentum, T the kinetic energy, m the mass, c the speed of light, Z the atomic number of the anode, r_0 the classical electron radius and α the fine structure constant.

To account for a detector element of area A_{d} at distance d, target self filtration and additional filtration, equation [3.2] needs to be modified:

$$N(h\nu)\,dh\nu = GH(h\nu)\,d_x n\left(\int_0^{\infty}\int_{h\nu/T_0}^{1}\frac{\Phi\left(h\nu,T_i(u)\right)}{T_i(u)}f(u,x)\,F\left(h\nu,x,\theta,\vec{r}\right)dudx\right)dh\nu\,, \quad [3.6]$$

where

$$G = \frac{A_{\mathrm{d}}}{4\pi d^2} \quad [3.7]$$

and

$$H(h\nu) = e^{-\sum_i \mu_i(h\nu)t_i}\,. \quad [3.8]$$

The subscript i in equation [3.8] refers to the different filtration materials of thicknesses t_i and linear attenuation coefficients μ_i. The function $F\left(h\nu,x,\theta,\vec{r}\right)$ accounts for the target's self attenuation. The target angle is represented by θ and $\vec{r}$ is the position of the detector element in a two dimensional plane at the detector level. The origin of the coordinate system is the point in the detector plane directly below the intersection of the x-ray beam and the target (see Fig. 8). The function $F\left(h\nu,x,\theta,\vec{r}\right)$ has been modified from the original model to better suit the needs of *ImaSim*:

$$F\left(h\nu,x,\theta,\vec{r}\right) = e^{-\mu(h\nu)s\left(x,\theta,\vec{r}\right)}\frac{d^2}{L\left(x,\theta,\vec{r}\right)^2}\,. \quad [3.9]$$

Fig. 8 shows the geometry of the target and illustrates the parameters found in equation [3.9]. The function $F\left(h\nu,x,\theta,\vec{r}\right)$ also accounts for the inverse square law correction needed for a flat detector. In *ImaSim* [3.9] is only applied in the cathode anode direction. The derivation for distances $s\left(x,\theta,\vec{r}\right)$ and $L\left(x,\theta,\vec{r}\right)$ is found in Appendix A.

Characteristic radiation is produced by electron impact ionization as explained in Section 2.1.3.1 and also by photoelectric absorption. Only K shell interactions are considered in *SpekCalc* and characteristic x-rays produced by electron impact inozation are modelled as a fraction of those from photoelectric absorption. The number of characteristic photons is thus:

$$N_{\mathrm{char}} = GH(1+P)\left(\frac{1}{2}f_{\mathrm{k}}\omega_{\mathrm{k}}\right)\sum_i \partial\left(h\nu - h\nu_i\right)\int_{h\nu_{\mathrm{k}}}^{T_0} N_{\mathrm{emit}}(h\nu)\,dh\nu \quad [3.10]$$

where P is the fraction of characteristic x-rays from impact ionization, f_k is the probability that an absorbed photon creates a vacancy in the K shell and ω_k is

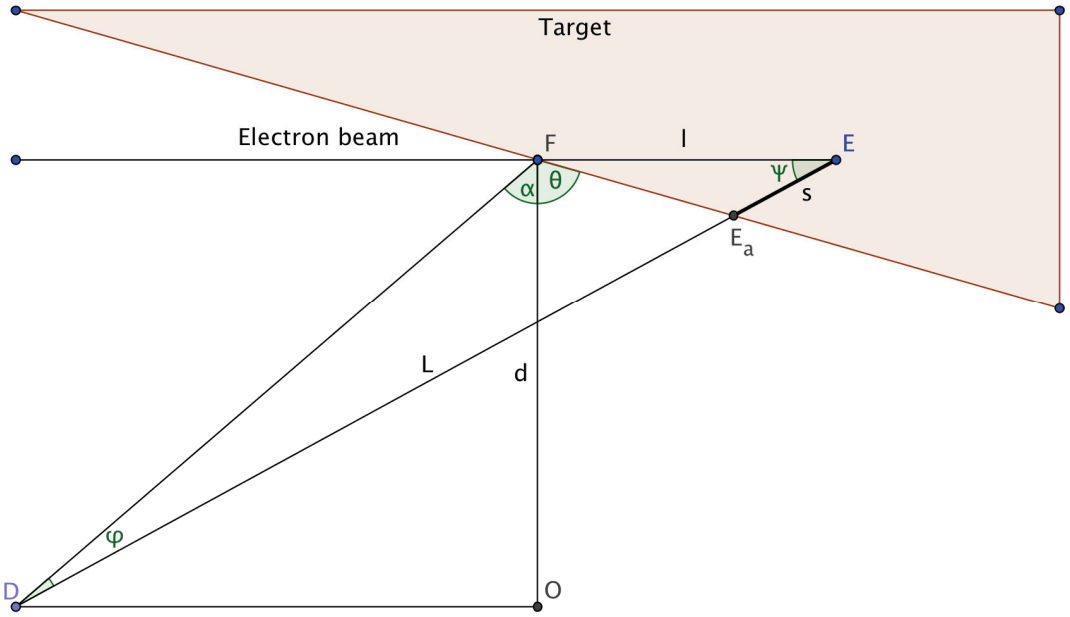

Figure 8: An electron travels to a depth l (or x) in a target with angle θ before emitting a photon at point E. The photon must go through a thickness s of material before reaching a detector element at point D, which is at a distance L from the emission point. The position of the detector element is specified by the angle α.

the probability that this vacancy leads to fluorescence. The $1/2$ factor accounts for the probability that a photon emitted near the surface of the target is absorbed. The K edge is given by $h\nu_k$ while T_0 designates the electron beam's energy. The subscript i designates the *i*th K line. This approach neglects target self filtration and is not as rigorous as the bremsstrahlung treatment. Given the small contribution of characteristic x-rays to the final spectrum, it is acceptable.

SpekCalc lets the user modify a number of parameters related to spectrum creation. They are listed in Table 2. Beside the x-ray spectrum, *SpekCalc* also provides the user with a series of beam characterization parameters listed on the following page.

- First and second half value layers (HVL)
- Homogeneity coefficient HVL_1/HVL_2
- Effective energy
- The above both in Al and Cu
- Mean energy
- Bremsstrahlung output
- Characteristic output

Some important details on HVL calculation are presented in Appendix B.

Parameter	Possible values
Peak energy (keV)	10 - 300
Energy bin size (keV)	Not limited
Target angle (degrees)	5 - 85
Filtration materials	Air Aluminum Beryllium Copper Tin Tungsten Water
Filter thickness (mm)	Not limited

Table 2: Parameters of the *SpekCalc* spectrum creation tool.

3.4.2 Megavoltage sources

Since *SpekCalc* only covers energies of up to 300 keV, megavoltage sources cannot be generated by it. In order to provide the user with the ability to study portal imaging, *ImaSim* has a library of megavoltage sources generated by MC simulations[3]. These sources cannot be modified.

3.5 Object Creation

ImaSim provides the user with the ability to image custom objects. These user created objects are made with an object editor containing a three dimensional viewing environment. Objects created in *ImaSim* are based on four different building blocks: rectangular prisms, elliptical cylinders, ellipsoids and right triangular prisms (see Fig. 9). An object consists of one or more of such building blocks. Each block has an assigned material with density and mass attenuation coefficients from the web database XCOM. They can be translated in three directions and rotated around three object axes. Multiple rotations are carried in order, with rotations around the x axis executed first, then around the y axis and finally around the z axis. The blocks also have three parameters each governing their size and shape.

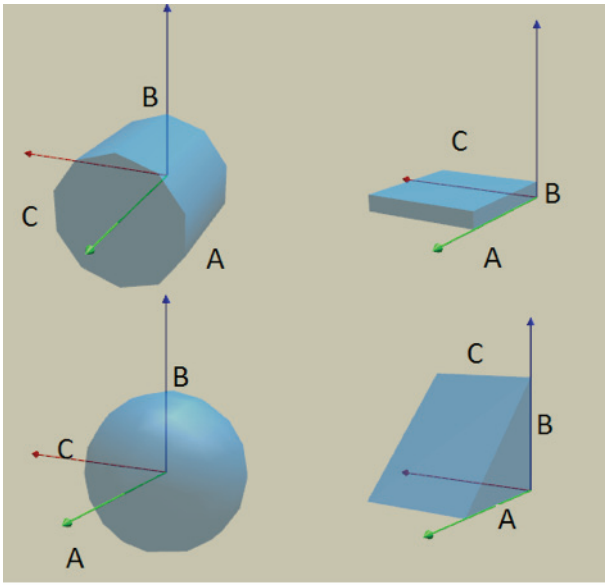

Figure 9: The four basic building blocks with their object rotation axes and shape parameters A, B and C. The x (y z) axis is green (red blue).

To account for overlap, blocks are assigned a priority number. Given two overlapping blocks, the intersection volume will have the physical properties of the higher priority block. It is also possible to assign a color and transparency to each block to make them distinguishable.

3.6 Geometrical Setup

Once a photon source and object have been selected, they need to be positioned in space with respect to a detector. *ImaSim* provides a three dimensional Cartesian coordinate system where this positioning takes place. The object has its own absolute coordinate system and the source and detector are positioned in another coordinate system, which can be translated with respect to the object's system. The goal is to provide the user with the freedom to create various imaging geometries.

Three different geometrical setup types are present in *ImaSim*: planar imaging, single slice CT and CBCT. In planar imaging, the beam covers a rectangular detector, forming a rectangular based pyramid. In single slice CT, the beam covers a one dimensional arc-shaped detector array, forming a fan. Finally in CBCT, the beam covers a square detector array, forming a square pyramid. The parameters for each case are listed and described in Table 3 to Table 5.

Parameter	Description
Source to origin distance (1)	The distance between the focal spot and the coordinate system's origin.
Detector to origin distance (1)	The distance between the detector's center and the coordinate system's origin.
Origin position (3)	The position of the origin with respect to the object.
Detector size (2)	The two dimensional size of the rectangular detector.
Number of detectors (1)	This governs the resolution of the image. To have isotropic resolution, the number of detectors is specified in one direction only.
Detector translation (2)	Translation of the detector only in the two dimensions perpendicular to the source to origin vector.
Source detector rotation (3)	Rotation of the source and detector system around the three axes of the coordinate system.

Table 3: Parameters of a planar imaging setup. Numbers in parenthesis represent the number of degrees of freedom associated with the parameter.

Parameter	Description
Source to origin distance (1)	*Idem*
Detector to origin distance (1)	*Idem*
Source detector rotation (3)	*Idem*
Origin position (3)	*Idem*
Fan angle (1)	The angular width of the fan beam.
Slice thickness (1)	In the case of a multiple slice scan, this sets the distance between slices.
Scan length (1)	When this parameter is larger than the slice thickness, more than one slice will be acquired.
Number of detectors (1)	This governs the resolution of the one dimensional array.
Number of views (1)	The number of projections around the object.

Table 4: Parameters of a single slice CT imaging setup. Numbers in parenthesis represent the number of degrees of freedom associated with the parameter.

Parameter	Description
Source to origin distance (1)	*Idem*
Detector to origin distance (1)	*Idem*
Source detector rotation (3)	*Idem*
Origin position (3)	*Idem*
Detector width (1)	The size of the square detector array.
Number of detectors (1)	The number of detectors along one side of the array. Governs resolution.
Number of views (1)	The number of projections around the object.

Table 5: Parameters of a CBCT imaging setup. Numbers in parenthesis represent the number of degrees of freedom associated with the parameter.

3.7 Detector Modelling

The geometrical arrangement of detector elements, their size and resolution are handled with the geometrical setup module presented in the previous sub-section. It is still necessary to model the x-ray absorption properties of detector arrays. The approach taken here is to associate an energy response curve to a given detector. An energy response curve gives the energy absorption of the detector throughout the spectrum, i.e. the mean fraction of an incident photon's energy deposited in a detector element. The response curve depends on the detector material and its thickness. A thicker detector (or higher Z) will absorb more energy than a thinner one (or lower Z). Response curves in *ImaSim* are either taken from the literature or simulated with MC. The MC simulation consists of a series of mono energetic sub simulations. In each sub simulation, an x-ray beam is impinging on a stack of slabs representing the composition of a given detector. A parallel beam is set up to cover a 40 x 40 cm^2 area of the detector and the dose is scored in the sensitive layer of the detector, over a 1 x 1 cm^2 central area representing a single detector element. The results of each mono energetic sub simulation can then be regrouped to create a response curve.

The simulations have been carried out with the DOSXYZnrc code which is part of the BEAMnrc MC package[4]. The parameters ECUT and PCUT were set to 0.700 and 0.01 MeV respectively. Rayleigh scattering, bound Compton scattering, electron impact ionization and atomic relaxation were off. Directional bremsstrahlung splitting was set to Koch-Motz. The number of simulated photons was 6×10^7.

3.8 Photon Transport and Detection

3.8.1 Ray tracing

Once a source, object and detector have been set up and positioned in space, it is possible to simulate the acquisition of x-ray transmission data. In order to fulfill the calculation speed requirements of Section 3.2, the photon transport model selected for *ImaSim* is ray tracing. In ray tracing, only photon

attenuation is considered and scattered photons are discarded. The objective of a ray tracing calculation is to obtain the radiological path l_r between source point A and detector point B. It is defined as follows:

$$l_r = \int_C \mu(s)\, ds \qquad [3.11]$$

where s defines the arc length along the straight curve C joining A and B. The number of mono energetic photons N_B reaching point B will then be:

$$N_B = N_A e^{-l_r} \qquad [3.12]$$

where N_A is the number of photons leaving point A. In the case of a poly energetic source, the radiological path needs to be calculated at every energy since the linear attenuation coefficient μ is energy dependent.

Since the objects of *ImaSim* are based on geometrical shapes, it is not necessary to transform them into three dimensional material arrays. The ray tracing algorithm used is not voxel based. Instead it uses the geometry of the four types of building blocks available. For a given ray, each block is checked for intersection with the ray and the radiological path is extracted for blocks that do intercept it.

3.8.2 Detection

The normalized signal associated to a detector element at point B is:

$$S_B = F \cdot \sum_i e^{-l_r(E_i)} \cdot E_i \cdot N(E_i) \cdot f(E_i) \qquad [3.13]$$

where $E \cdot N(E)$ is the enegy fluence for the spectrum bin centered at energy E, $f(E)$ is the energy response of the detector at that energy and F is a normalization factor:

$$F = \frac{1}{\sum_i N(E_i) \cdot E \cdot f(E_i)}. \qquad [3.14]$$

In a simulation, the radiological path is calculated at every source point-detector point pairs and at every energy. To limit calculation time, a single source point is generally used. Another approximation consists of considering the

intensity reaching the central point of a detector element as the average intensity over its area.

3.9 Data Processing

Once detector signals have been acquired, some further data processing may be required to obtain an image. In the case of kV or MV planar imaging, the normalized detector signal constitutes the final image. A renormalization may be applied, but such data processing is trivial. In the case of CT and CBCT, more intensive data processing is necessary.

3.9.1 CT

As seen in Section 3.6, the detector in CT is arc shaped and is illuminated by a fan beam of x-rays. The raw data consists of a series one dimensional projection images taken over 360 degrees. The data is stored in a two dimensional matrix called sinogram. The sinogram space is a two dimensional projection space where the horizontal axis represents the tube angles β and the vertical axis the detector element positions specified by angle α. Detectors are specified by an angle due to the fan geometry (see Fig. 10).

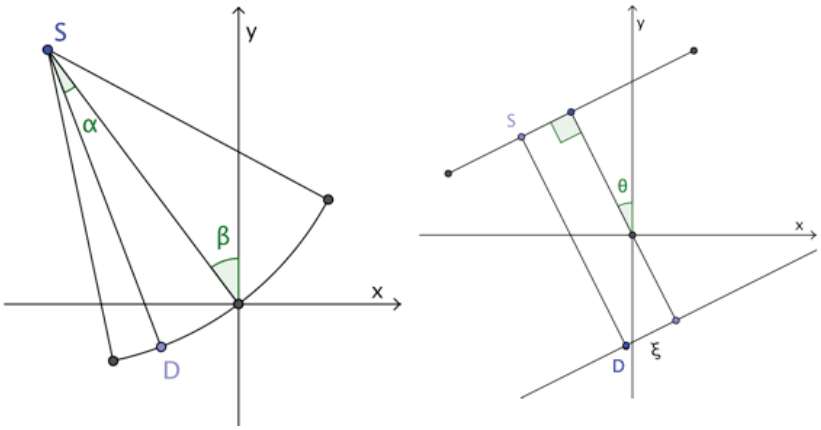

Figure 10: Fan beam geometry (left) with source at point S and detector at point D. Angle β represents the tube angle and angle α a detector position in the curved detector array. The detector array is drawn at the point of rotation but is usually at a distance from it. In parallel beam geometry (right) the tube angle is specified by θ and ξ specifies a detector position in the linear detector array.

3.9.1.1 Fourier transform

Data processing in CT makes heavy use of the Fourier transform. Since the data is discrete, the actual transform used is the discrete Fourier transform (DFT). It is possible to rapidly calculate DFTs with fast Fourier transform (FFT) algorithms. To use such algorithms, the number of data points needs to be a power of 2. Arrays are thus zero padded to the next power of 2 when required. The algorithm used in *ImaSim* is taken from Numerical Recipes in C[5].

3.9.1.2 Sinogram conversion

The backprojection algorithm presented in Section 2.2.2 is based on the parallel beam geometry while the sinogram data from the simulation are from a fan beam. It is thus necessary to convert the fan sinogram to a parallel sinogram where the horizontal axis is the angle θ and the vertical axis becomes the detector spatial position ξ along the flat detector array (Fig. 10). This is feasible since for a given tube angle β, a ray specified by α can be associated to an equivalent ray in the parallel geometry at some tube angle θ and position ξ. The equivalent ray has the following coordinates:

$$\xi = R\sin\alpha \qquad [3.15]$$

and

$$\theta = \beta + \alpha \qquad [3.16]$$

where R is the source to detector distance in the fan geometry. It is thus possible to do a two dimensional interpolation of the parallel sinogram from the fan sinogram. This can be achieved by shifting every horizontal line in the fan sinogram by its angular position α. A line with positive α would be shifted to the left and lines with larger α undergo a greater shift than those with smaller α. This fulfills the requirements of equation [3.16]. We see from equation [3.15] that data in the vertical direction is not sampled at a regular interval with respect to ξ since the sampling is regular with respect to α. It is thus necessary to interpolate it on a regular grid. This shift and interpolate approach was presented by Pan[6].

The shifting is done by taking the Fourier transform of each horizontal line and multiplying it by a shift factor $e^{-ik_\beta \alpha}$ where k_β is the frequency associated with β. The interpolation is done in the Fourier space and the inverse transform yields the parallel sinogram.

3.9.1.3 Filtering

A. Filter selection

The next step consists of filtering the projections. *ImaSim* provides the ramp filter, also called Ram Lak filter, which was presented in Section 2.2.2. Filtering can also be done with filters which reduce the high frequency content of the projections. This is desirable in the presence of high frequency noise and has a blurring effect on the final image. Two such filters are included in *ImaSim*: the Shepp Logan filter and cosine bell filter[7]. The filters are shown in Fig. 11. They are described mathematically by:

$$F(k)_{\text{RamLak}} = |k|, \qquad [3.17]$$

$$F(k)_{\text{SheppLogan}} = \frac{|k| \sin\left(\frac{k\pi}{k_{\max}}\right)}{k\pi} \qquad [3.18]$$

and

$$F(k)_{\text{cosine}} = |k| \cos\left(\frac{k\pi}{k_{\max}}\right) \qquad [3.19]$$

where $k_{\max}$ is the largest spatial frequency, defined by the data spacing in the parallel sinogram:

$$k_{\max} = \frac{1}{2}\frac{N}{D} \qquad [3.20]$$

where N is the number of detectors and D is the width of the detector array. It is also possible to do the backprojection without applying a filter to visualize the $1/r$ blurring.

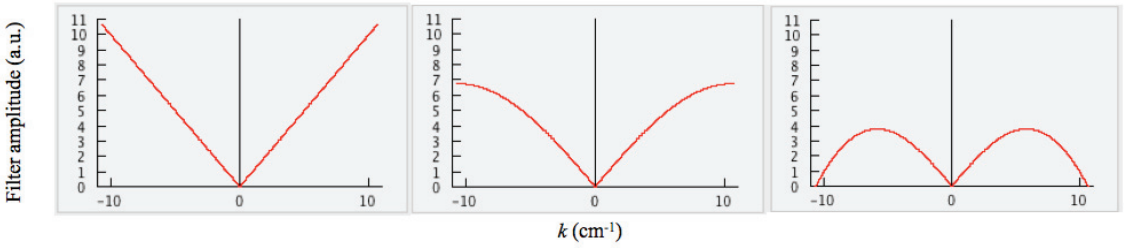

Figure 11: Filters available in *ImaSim*. From left to right: Ram Lak, Shepp Logan and cosine bell filters.

B. Zero padding

The filtering done in the Fourier space corresponds to a convolution in projection space. It is well known that the convolution obtained by using a DFT is cyclic. This can lead to aliasing artefacts in the convoluted projections, caused by overlap of the outermost data.

It can be assumed that the original data falls off to zero before the edges of the detector. It is then band limited in the projection space. Taking a forward then inverse FFT on such data would yield no artefacts. However, the application of a filter to the Fourier transformed projections modifies their spectral content. The new filtered projections, obtained by the inverse Fourier transform, may now extend beyond the original detector width. This in itself is not a problem for image reconstruction, since the data found outside the detector width is irrelevant for image formation. The problem stems from the cyclic nature of the convolution. Since the filtered projections are now wider than the arrays containing them, data at the edges will be contaminated by the next period in an additive way. The artefact this introduces in the final image is called dishing[8].

Another artefact, more subtle, comes from the zero frequency value in the FFT of the projections. The filter's shape dictates that the $k = 0$ frequency only should have zero contribution. The sampling process makes it so that the whole bin centered on zero is considered to have zero contribution. This creates a DC artefact[8].

The dishing artefact can be removed by zero padding the projections prior to filtering. This will provide enough room for the relevant portions of the filtered projections not to overlap. If N data points are present, then it is required to

zero pad to $2N-1$ to eliminate the dishing artefact. Of course, to use the FFT, power of 2 array sizes are required. ImaSim provides the user with the option to pad to a given power of two size with a parameter called zero pad order. Table 6 shows how detector arrays of different sizes are zero padded with respect to the zero pad order parameter.

	Zero pad order			
	0	1	2	3
60 detectors	64	128	256	512
64 detectors	64	128	256	512

Table 6: Sizes of zero padded projections.

Zero padding increases the sampling rate in the Fourier domain. This has the effect of diminishing the size of the bin centered on zero and reducing the DC artefact. Technically this artefact can never be totally eliminated, since the bin size around zero will always be finite.

3.9.1.4 Backprojection

The filtered projections are used to reconstruct the image with the backprojection method of Section 2.2.2. Given the parallel geometry, only projections between 0 and 180 degrees need to be used. Once the backprojection is complete, the attenuation values are ready to be converted into HU.

3.9.1.5 Conversion to HU

To be able to convert the result of the backprojection to HU, knowledge of μ_{water} is required. In the case of a mono energetic beam, the identification of μ_{water} is trivial. However, when dealing with a poly energetic beam, it is more difficult to identify the correct value since μ_{water} varies with energy. One could be tempted to

use the μ_{water} corresponding to the mean energy of the beam, but this is not a viable solution since this mean energy varies with depth due to beam hardening.

This variation has a marked effect on the reconstructed image. Without correction, the reconstructed image of a uniform water cylinder scanned with a poly energetic beam will have non uniform values across its diameter. This is called the cupping artefact. It is thus impossible to assign a correct value to μ_{water} since it varies with position in the image. In *ImaSim*, μ_{water} is obtained by reconstructing a uniform water cylinder whose radius is ¾ of the field of view (FOV) radius. This radius is chosen to reproduce the filling of the FOV in a regular scan. The FOV is the circular area corresponding to the intersection of all the projection beams. The value for μ_{water} is taken at half the radius of this reconstructed cylinder and there will be cupping in the image.

3.9.1.6 Correction for beam hardening

A primitive beam hardening correction algorithm is included in *ImaSim*. The algorithm is based on the assumption that the geometry being imaged is cylindrical and made of water. The user specifies the radius r of a water cylinder, which should match the object being imaged and the algorithm calculates the path length l in water of a ray reaching a detector specified by d in parallel geometry (Fig. 12):

$$l(d) = 2\sqrt{r^2 - d^2}\ . \qquad [3.21]$$

With knowledge of the spectra, it is possible to calculate an ideal projection p_i:

$$p_i(d) = \frac{\sum_i \mu_{\text{water}}(E_i) \cdot l(d) \cdot N(E_i) \cdot E_i \cdot f(E_i)}{\sum_i N(E_i) \cdot E_i \cdot f(E_i)}, \qquad [3.22]$$

which is simply a weighted sum over $\mu_{water}(E_i)$, and the real projection p_r:

$$p_r(d) = -\ln \frac{\sum_i N(E_i) \cdot e^{-\mu_{\text{water}}(E_i) \cdot l(d)} \cdot E_i \cdot f(E_i)}{\sum_i N(E_i) \cdot E_i \cdot f(E_i)}. \qquad [3.23]$$

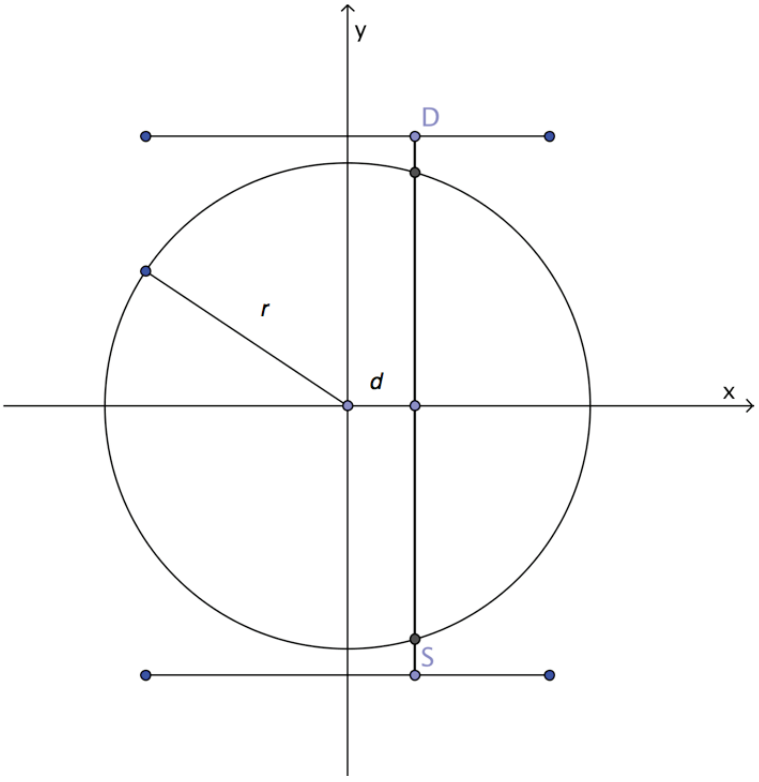

Figure 12: Geometry for the beam hardening correction. The cylinder of radius r is water, the ray from source S to detector D is at a distance d from the origin.

The ideal projection ignores beam hardening and reconstructing the water cylinder from it yields a uniform image where there is no cupping and where μ_{water} is extracted. Dividing equation [3.22] by equation [3.23] yields a correction curve which can be applied to the projections from the geometry being imaged. Of course this correction is only valid for objects which are cylindrical in shape and mostly water equivalent.

3.9.2 CBCT

In CBCT, no geometry conversion is required. The theory presented in Section 2.2.3 is directly applied to reconstruct the image. The discussions on Fourier transforms and filtering of Section 3.9.1 also apply here: to obtain a reconstructed image, the user selects a filter and the order of zero padding. An additional input is required to obtain the final image: given the three dimensional nature of CBCT, the user needs to specify the position and orientation of the

reconstructed slice. A slice can thus be axial, sagittal or coronal and be positioned anywhere in the reconstruction volume. Full three dimensional reconstruction is not implemented in *ImaSim* because of long calculation times. The values of μ_{water} are obtained by a simple weighted average:

$$\mu_{\text{water}} = \frac{\sum_i \mu_{water}(E_i) \cdot N(E_i) \cdot E_i \cdot f(E_i)}{\sum_i N(E_i) \cdot E_i \cdot f(E_i)}. \qquad [3.24]$$

No beam hardening correction is provided for CBCT.

3.10 Image Study

3.10.1 Main tools

Once images have been created with one of the four modalities, they can be viewed with an image viewing tool. This module lets the user inspect images in a quantitative way with a number of tools. These tools and other capabilities of the image viewer module are listed below:

- Modify window width and level
- Pick color scale
- Inspect value and pixel position
- Draw line region of interest (ROI) providing length
- Obtain profile plot from line ROI
- Oval and square ROI providing area, mean and standard deviation
- Obtain value histogram plot from oval and square ROI

A number of mathematical operations are also available:

- Sum of two images
- Difference of two images
- Product of two images
- Quotient of two images
- Normalization of a single image
- Background subtraction of single image
- Re-grid single image with nearest neighbour interpolation

- Re-grid single image with bilinear interpolation
- Gamma comparison of two images in 2D

When two images of different resolution are used in a mathematical operation, bilinear interpolation is used to resample them onto the grid of the higher resolution image. Images have isotropic resolution.

3.10.2 Gamma comparison

Gamma comparison is a dose distribution comparison method taking into account not only dose differences but also shifts in the dose distribution[9]. It compares a measured image to a calculated or reference image and yields a comparison image called a gamma map. Given a dose difference criterion ΔD and a distance to agreement (DTA) criterion Δd, the gamma map $\gamma(\vec{r}_{\mathrm{m}})$ is given by:

$$\gamma(\vec{r}_{\mathrm{m}}) = \min\left\{\Gamma(\vec{r}_{\mathrm{m}}, \vec{r}_{\mathrm{c}})\right\} \forall \{\vec{r}_{\mathrm{c}}\} \qquad [3.25]$$

where

$$\Gamma(\vec{r}_{\mathrm{m}}, \vec{r}_{\mathrm{c}}) = \sqrt{\left(\frac{|\vec{r}_{\mathrm{m}} - \vec{r}_{\mathrm{c}}|}{\Delta d}\right)^2 + \left(\frac{D(\vec{r}_{\mathrm{m}}) - D(\vec{r}_{\mathrm{c}})}{\Delta D}\right)^2}\ . \qquad [3.26]$$

Positions in the reference image are specified by $\vec{r}_{\mathrm{c}}$ and positions in the measured image are specified by $\vec{r}_{\mathrm{m}}$. The dose difference criterion can be set as a fixed value or as a percentage of the local dose value in the reference image. The gamma map shows where the measured image fails both dose difference and DTA criterions. It also quantifies the failure by providing a value larger than unity for failing pixels. In *ImaSim*, the gamma map does not compare dose values, instead it looks at differences in pixel values.

The gamma map calculation in ImaSim follows the approach of Stock et al[10]. The first step consists of re-interpolating both images onto a common grid. The grid size is specified by the user, as well as the dose difference and DTA criterions. The user also specifies a search range for the minimization. This search range is usually of the order of a few DTAs to keep calculation times

acceptable. The algorithm first measures the value $\Gamma(\vec{r}_m, \vec{r}_c)$ at $\vec{r}_c = \vec{r}_m$. It then calculates $\Gamma'(\vec{r}_m, \vec{r}_c)$ at one of the four pixels closest to $\vec{r}_m$:

$$\Gamma'(\vec{r}_m, \vec{r}_c) = \sqrt{\frac{|\vec{r}_m - \vec{r}_c|^2}{\Delta d^2}} . \qquad [3.27]$$

If this value is larger than $\Gamma(\vec{r}_m, \vec{r}_c)$ at $\vec{r}_c = \vec{r}_m$ then the search is stopped since no other point can have a smaller value. Otherwise the minimum is found in the area covered by the square ring of pixels surrounding $\vec{r}_m$ and $\Gamma'(\vec{r}_m, \vec{r}_c)$ is then calculated at one of the four pixels closest to $\vec{r}_m$ in the next square ring of pixels. The steps described above are repeated until the minimum is found or the square pixel rings become larger than the search range.

3.11 Summary of Operation

In the previous sections, the modules governing the simulation parameters have been presented. These modules are interrelated and their relationships are shown in Fig. 13. It shows and describes the logic flow required to obtain an image.

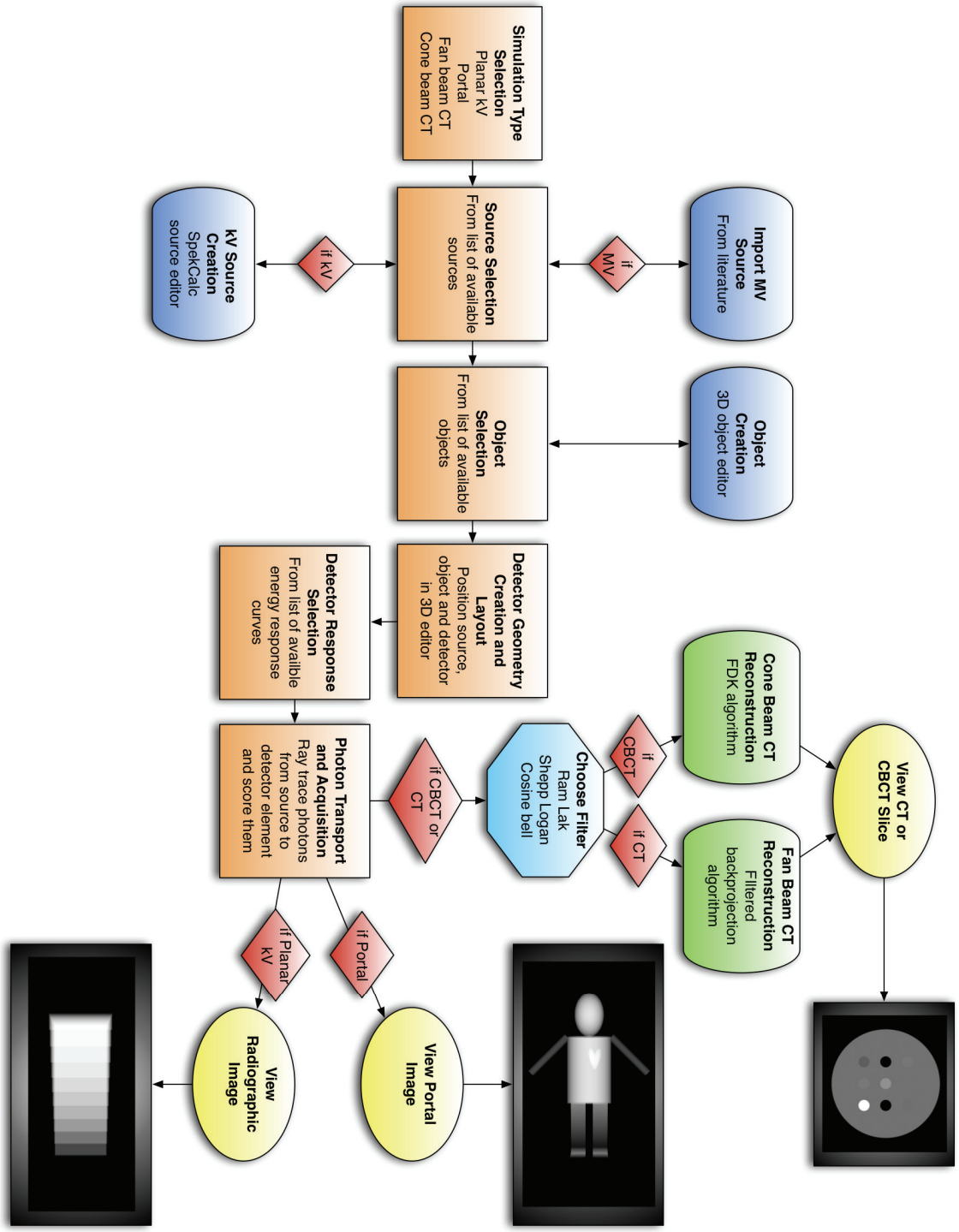

Figure 13: Flowchart presenting the steps required to obtain a simulated image and the relationships between the various modules of *ImaSim*.

REFERENCES

[1] G. Poludniowski and P. Evans, "Calculation of x-ray spectra emerging from an x-ray tube. Part I. Electron penetration characteristics in x-ray targets," Medical Physics **34**, 2164-2174 (2007).

[2] G. Poludniowski, "Calculation of x-ray spectra emerging from an x-ray tube. Part II. X-ray production and filtration in x-ray targets," Medical Physics **34**, 2175-2186 (2007).

[3] R. Mohan, C. Chui and L. Lidofsky, "Energy and angular distributions of photons from medical linear accelerators," Medical Physics **12**, 592-597 (1985).

[4] D. W. O. Rogers, B. A. Faddegon, G. X. Ding, C. Ma and J. We, "BEAM: A Monte Carlo code to simulate radiotherapy treatment units," Medical Physics **22**, 503-524 (1995).

[5] W. H. Press, S. A. Teukolsky, W. T. Vetterling and B. P. Flannery, *Numerical Recipes in C*. (Cambridge University Press, Cambridge, 1992).

[6] X. Pan, "Optimal noise control in and fast reconstruction of fan-beam computed tomography image," Medical Physics **26**, 689-697 (1999).

[7] T. M. Buzug, *Computed Tomography*. (Springer, Berlin, 2008).

[8] A. C. Kak and M. Slaney, *Principles of Computerized Tomographic Imaging*. (Society of Industrial and Applied Mathematics, 2001).

[9] D. A. Low, W. B. Harms, S. Mutic and J. A. Purdy, "A technique for the quantitative evaluation of dose distributions," Medical Physics **25**, 656-661 (1998).

[10] M. Stock, B. Kroupa and D. Georg, "Interpretation and evaluation of the γ index and the γ index angle for the verification of IMRT hybrid plans," Physics in Medecine and Biology **50**, 399-411 (2005).

CHAPTER 4: RESULTS

4.1 Graphical User Interface

4.1.1 Simulation window

As explained in the previous chapter, *ImaSim* takes the user through a series of modules related to image formation. These modules are linked together by the simulation window, which provides the user with the ability to select a spectrum, geometrical object, geometrical setup and detector response curve from libraries of such items. For each selection except detector response curve, it is possible to open an editor and create custom sources, object or setup geometries. It is also possible to visualize a plot of the detector response curve as well as its effect on the photon spectrum. The simulation window is shown in Fig. 14. In the case of planar kilovoltage imaging, some simulation settings such as the inclusion of focal spot size or heel effect can also be selected.

4.1.1 Editors

The editors all have their own windows. The editors provide control over the parameters presented in sections 3.4, 3.5 and 3.6 and give visual feedback with spectrum plots and three dimensional environments. Sources, objects and setups created with the editors can be saved and become available to the simulation window. The kilovoltage source editor is shown in Fig. 15. The input parameters related to source creation have been presented in Table 2. The editor provides a spectrum plot as well as the parameters listed in Section 3.4.1. The object editor is shown in Fig. 16 where we see an example object. The object editor displays, in the components list, the list of building blocks used to create the final object. Each of these blocks can be modified and their order in the components list corresponds to their priority number, as defined in Section 3.5. The final editor, which handles the geometrical setup, is shown in Fig. 17.

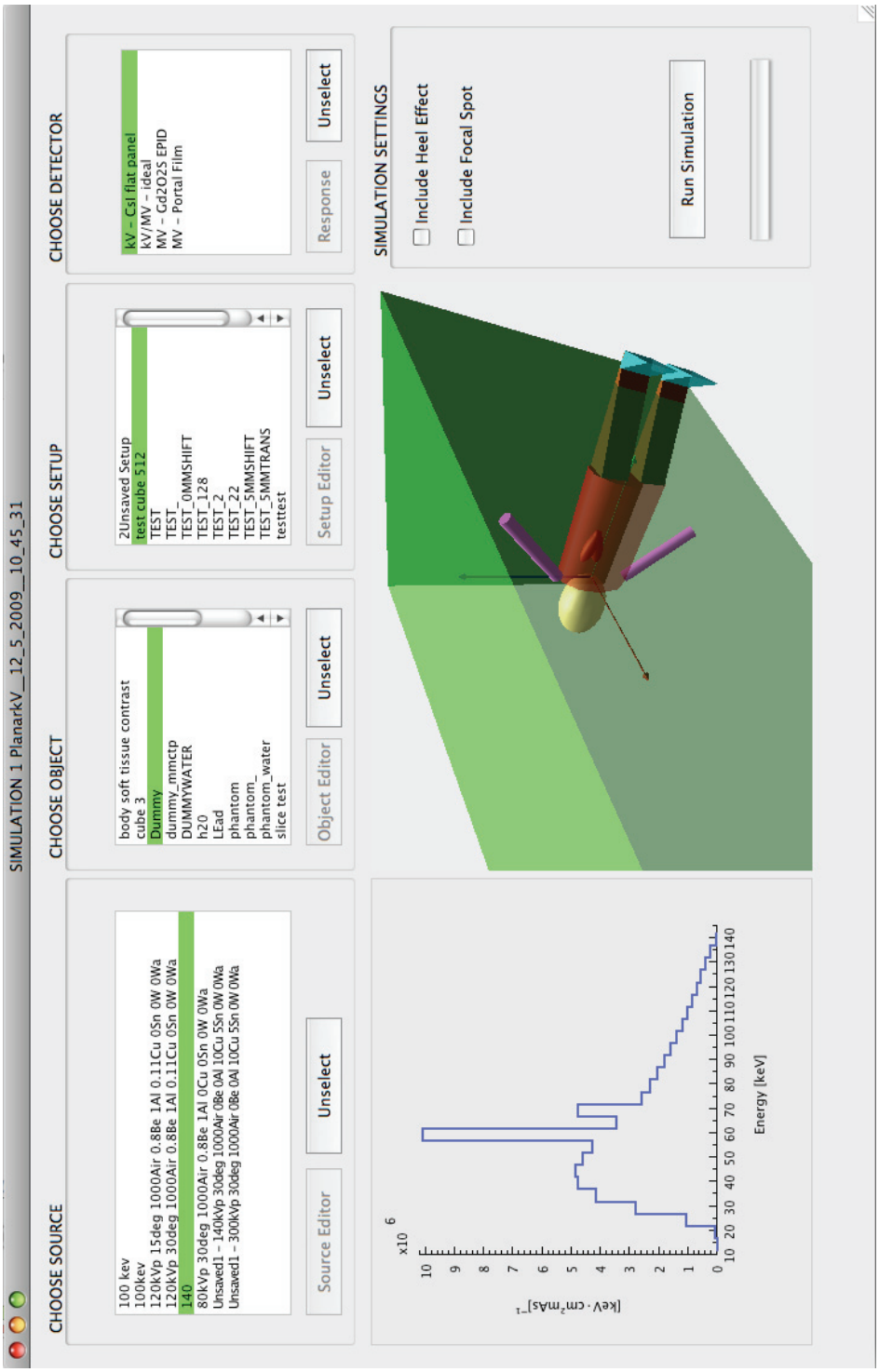

Figure 14: The simulation window in *ImaSim*. This window controls all the parameters relevant to the imaging simulation. The simulation window provides feedback to the user by displaying a plot of the selected spectrum as well as a three dimensional environment with object and geometrical setup.

The editor's three-dimensional environment displays the source, beam, detector and object with different colors and relevant shapes. There are three variations of the setup editor: planar imaging setup editor, CT setup editor and CBCT setup editor. Each variant represents the geometrical situation associated with the selected modality.

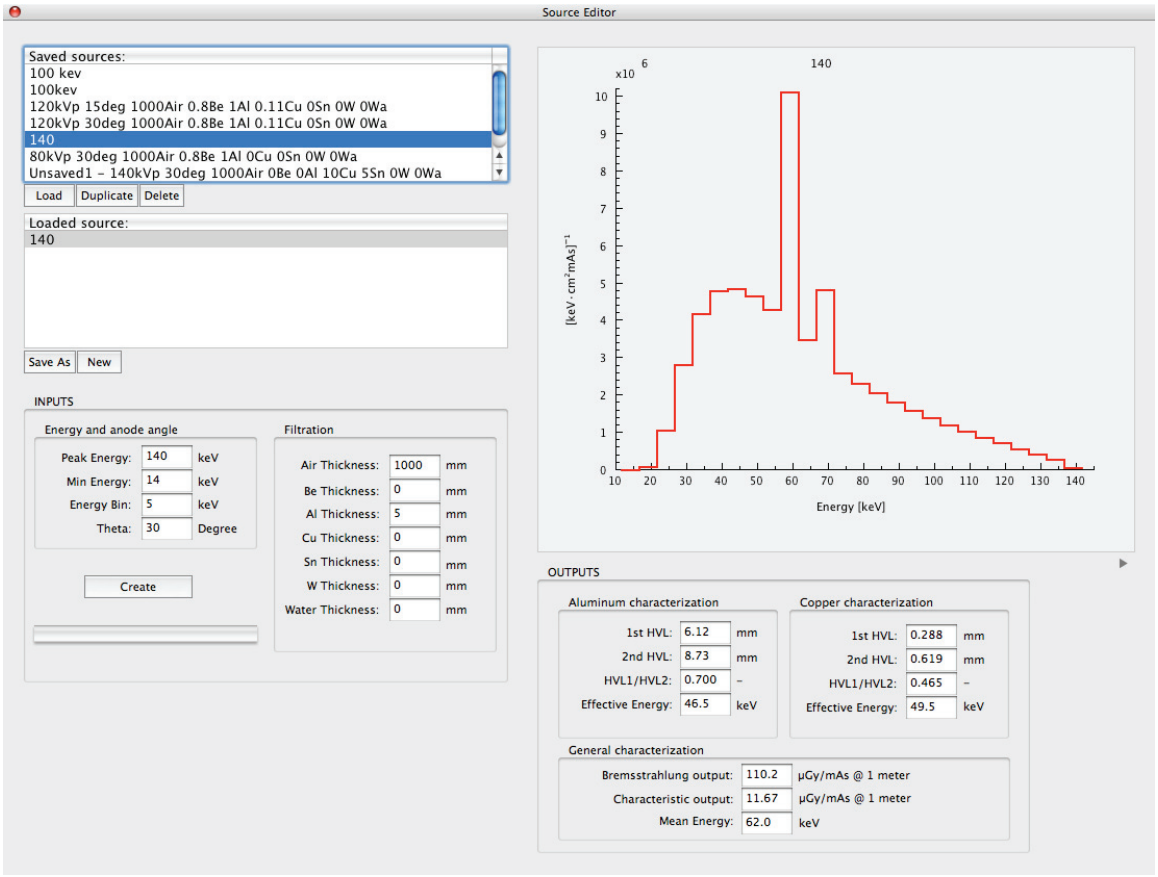

Figure 15: The kilovoltage source editor. After receiving the necessary inputs, it calculates a spectrum with the *SpekCalc* model and provides visual feedback.

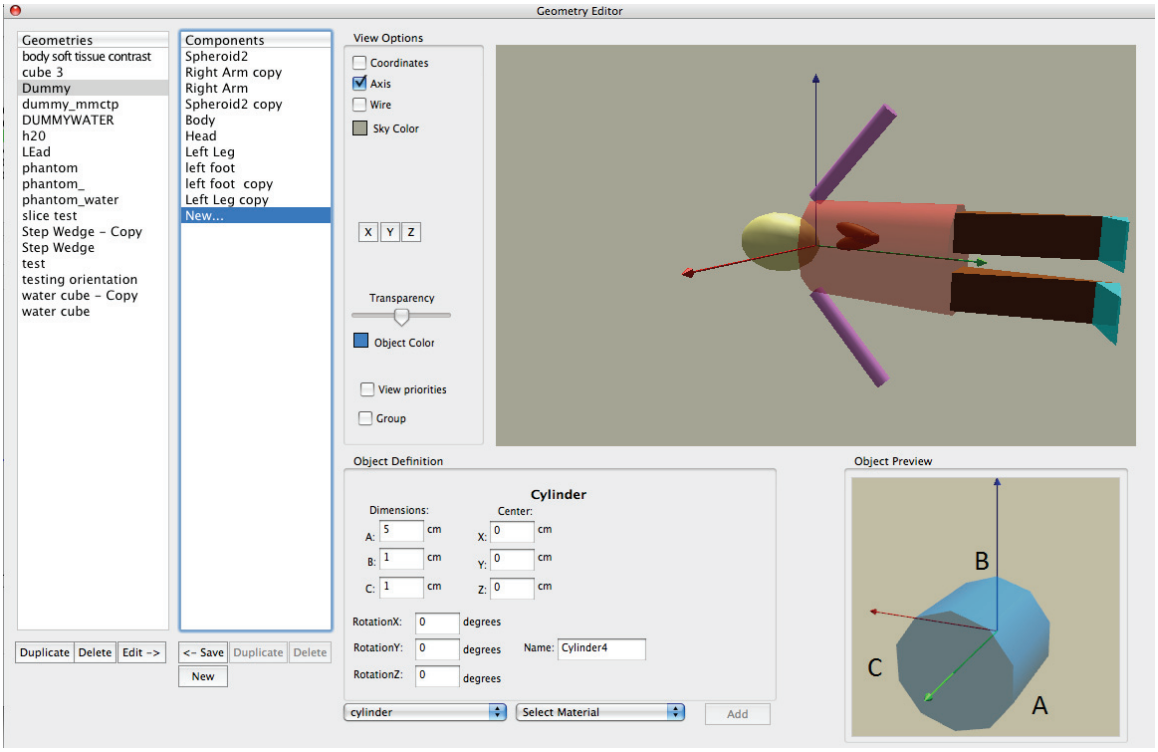

Figure 16: The object editor is shown here. Each object is a collection of building blocks having their own parameters. A color, transparency, material, position, name as well as dimensions can be assigned to each block in the three dimensional environment.

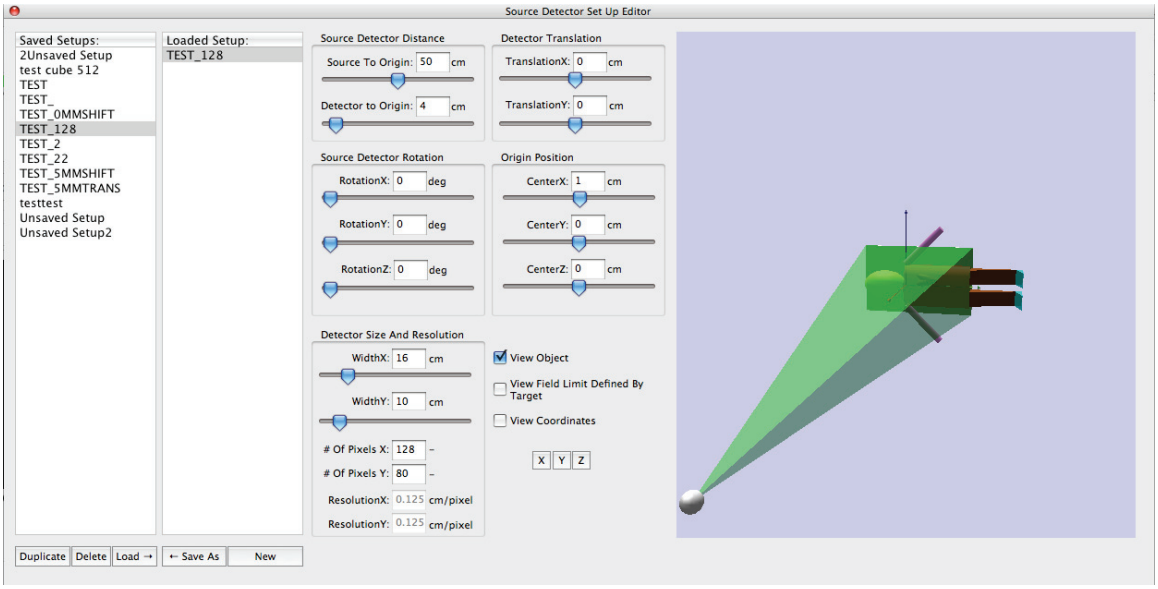

Figure 17: The setup editor for planar imaging is shown here. Parameters are varied interactively with sliders and their effect on the setup are shown in the three dimensional environment. Visible are the source (sphere), beam (pyramid), detector (plane) and object.

4.1.2 Detector response

ImaSim provides the user with a detector response curve inspector. This is a simple window where the response curve is plotted. The response curve can be shown in the energy range covered by the selected spectrum or over the whole available data range. It is also possible to display the spectrum and the effective spectrum. The effective spectrum is the original spectrum weighted by the detector response curve. This inspector is shown in Fig. 18.

All curves shown in the inspector are normalized to unity to facilitate viewing. The curve in Fig. 18 has been obtained from MC calculations described in Section 3.8.2. The detector modeled is a CsI based CBCT flat panel detector.

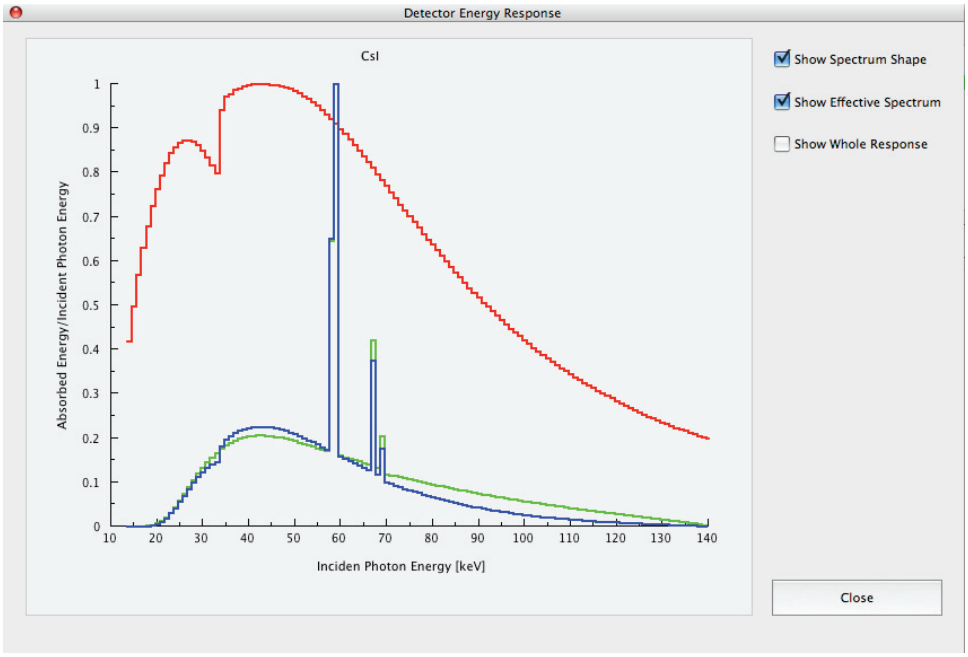

Figure 18: The detector energy response inspector. Shown are the energy response of a CsI flat panel detector for CBCT imaging (red), the original spectrum (green) and effective spectrum (blue).

4.1.3 Data processing

In the case of planar kV or MV imaging, running the simulation yields the final image and no further processing is required. Such images will be presented in a later section.

4.1.3.1 CT

Once photons have been transported in CT, the simulation window displays the fan sinogram. By pressing a button, the user then converts this fan sinogram to a parallel sinogram. The fan and parallel sinograms are shown in Fig. 19. A geometry exaggerating the difference between the two sinograms has been selected. The effects of the shift along the horizontal direction and interpolation along the vertical direction are visible. After the conversion, the user is able to select a filter, the zero pad order and image size for the backprojection. It is also possible to enable the beam hardening correction.

Figure 19: Sinogram conversion in ImaSim. The fan sinogram (top) is converted to a parallel sinogram (bottom). The effect is amplified by using an 80 degree fan angle.

4.1.3.2 CBCT

In CBCT, it is not possible to display a sinogram since we have a two dimensional array for each tube position. *ImaSim* displays these projections and lets the user scroll through them using the mouse. Following the filter and zero pad selection, the filtered projections are displayed. With the help of a three dimensional environment, the position of the reconstruction slice is then selected and the backprojection done. Fig. 20 illustrates these steps.

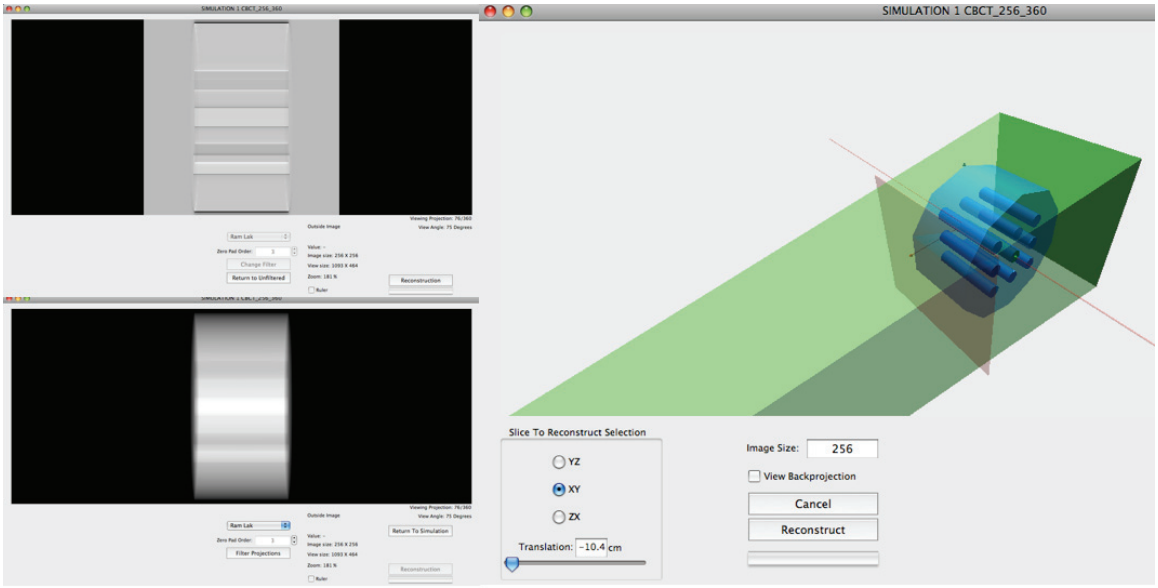

Figure 20: The various data processing steps of CBCT. Clockwise from bottom left are: projections, filtered projections and reconstruction slice (red plane) positioning.

4.2 Images

The main purpose of *ImaSim* is the creation of virtual medical images. After going through the modules presented in the previous section, the GUI provides the user with the result of the simulation: the image. The image viewer, shown in Fig. 21, provides the user with the ability to inspect images. Its functions have been described in Section 3.10.

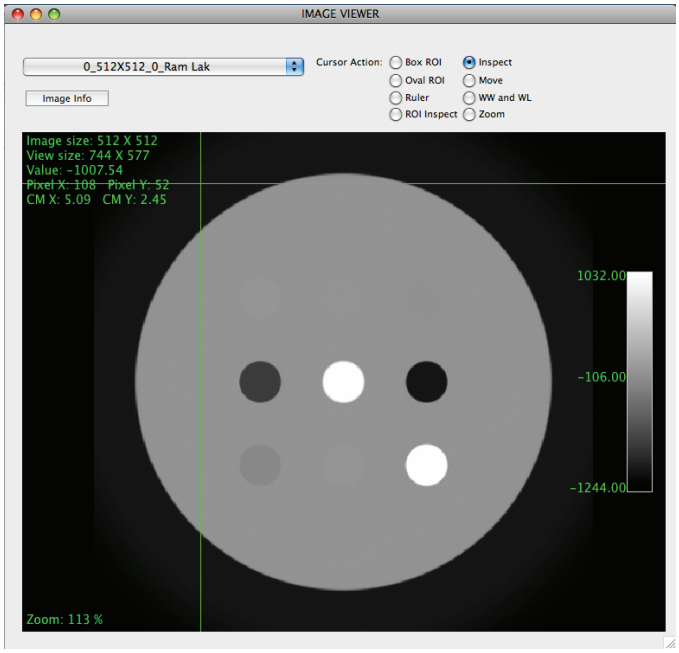

Figure 21: The image viewer window provides information on the loaded image.

4.2.1 Planar images

The images provided by a planar imaging simulation are two dimensional projections images. Examples of such images are given in Fig. 22. A rudimentary human body phantom as well as a step wedge polymethyl methacrylate (PMMA) phantom has been virtually imaged using *ImaSim*. Black regions correspond to areas that received the highest number of photons while white regions correspond to those that received less. These images show the versatility of *ImaSim* in creating and imaging varied geometries. Images created by using MV sources are similar to those obtained from kV sources. The main difference is a reduced contrast due to the dominance of the Compton effect. This difference is better evaluated by quantifying contrast than by a qualitative assessment obtained by visually comparing images. Such comparisons will be done in a later section.

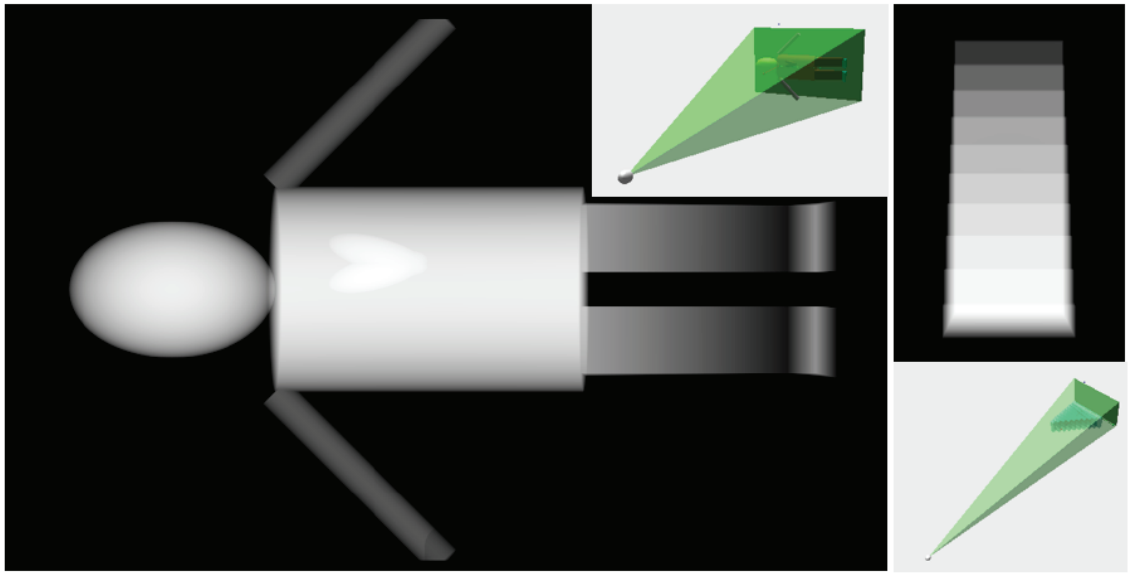

Figure 22: Images created with a kilovoltage planar imaging simulation. A tube potential of 140 kVp was used. The heel effect and focal spot size have been neglected. The insets show the geometrical object being imaged as well as the setup.

4.2.2 CT images

The result of a CT simulation is a cross sectional HU map of the object being imaged. Such an image is presented in Fig. 23 where a cylindrical water phantom containing smaller cylindrical inserts has been imaged. White regions correspond to high HU values, or high attenuation. They are typically bony structures. The dark regions correspond to low HU values, generally air or lung. The image of Fig. 23 has been taken with a mono energetic beam to minimize artefacts related to beam hardening. Such artefacts will be presented in a later section. The data has been acquired with 512 detectors over 1024 tube positions.

4.2.3 CBCT images

Once CBCT data has been filtered, it is possible to reconstruct any point in the three dimensional reconstruction volume. In *ImaSim*, these points are regrouped in slices which can be axial, sagittal or coronal. The slices can be positioned anywhere as mentioned earlier. As in CT, the values in a CBCT image are HU.

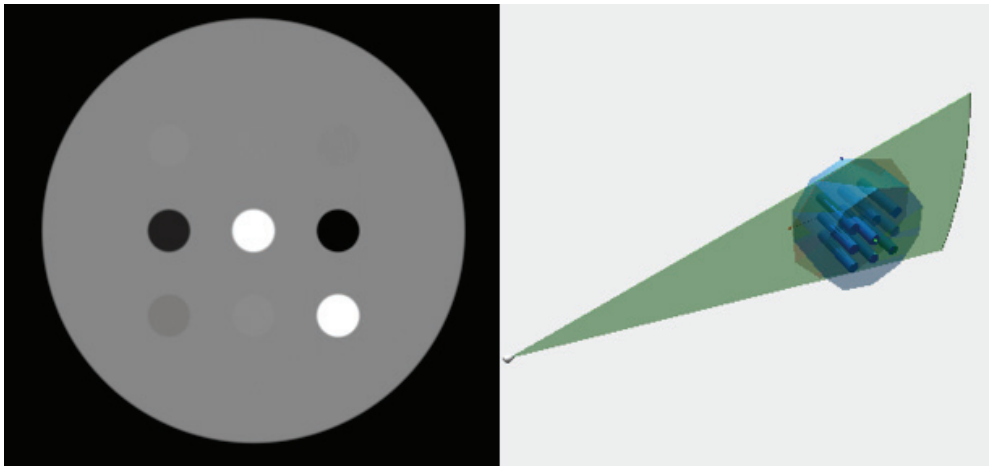

Figure 23: Result of a CT simulation. This cross sectional image (left) is a HU map of a water cylinder with smaller cylindrical inserts (right). The image has been taken with a mono energetic 100 keV beam and reconstructed with the Ram Lak filter.

Fig. 24 shows reconstructed images of the same phantom described in the CT section. We see the three different slice orientations. The data has once again been acquired with a mono energetic beam to minimize artefacts. The setup consisted of 256 detectors and 360 tube positions.

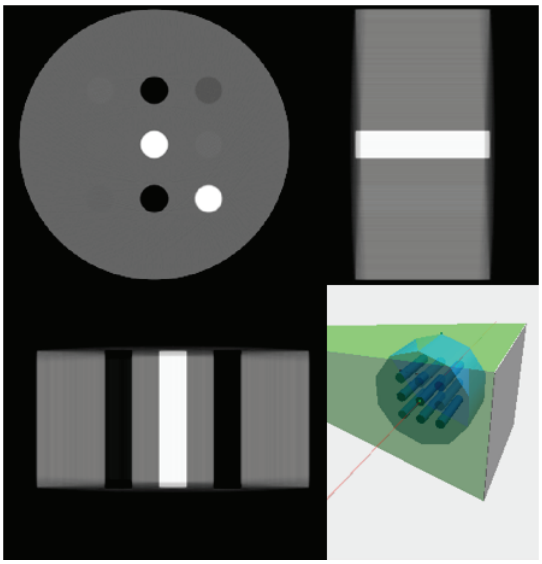

Figure 24: Results of a CBCT simulation. Counterclockwise from top right: coronal, axial and sagittal slices, as well as the imaging setup and phantom. The image has been taken with a mono energetic 100 keV beam and reconstructed with the Ram Lak filter.

4.3 Demonstrable Phenomena

The previous section showed that *ImaSim* can be used to create virtual images of user created geometries. It can also be used to illustrate some more subtle phenomena related to x-ray imaging. Some case studies will be presented here and will highlight the capabilities of *ImaSim*. They will be presented by modality.

4.3.1 Planar kilovoltage imaging phenomena

4.3.1.1 Beam hardening

Beam hardening has been presented in Section 2.1.4.6. Fig. 3 illustrates various spectra filtered with various thicknesses of aluminum. These spectra have been generated with *ImaSim* using *SpekCalc*. Fig. 25 shows that the mean energy and HVL of these spectra increases with the amount of filtration placed in the beam. Such an increase signifies that the beam becomes more penetrating due to the removal of low energy components.

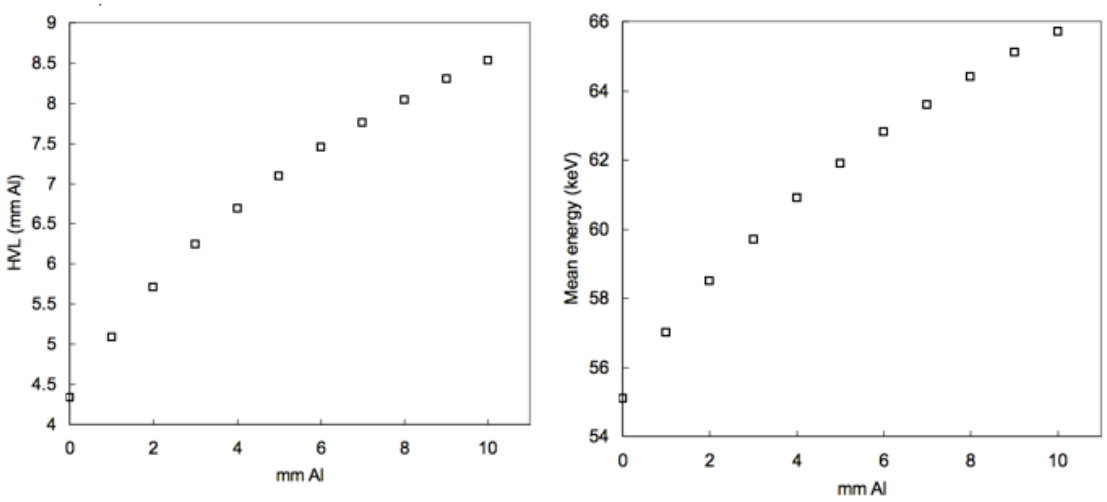

Figure 25: Mean energy (right) and HVL (left) of a 120 kVp photon beam after various thicknesses of aluminum filtration illustrating beam hardening. Produced with a 30 degree tube angle with 0.8 mm Be and 0.1 mm Cu initial filtration.

4.3.1.2 Heel effect and off axis spectral effects

With the modifications to *SpekCalc* presented in Section 3.4.1, a user is able to take the heel effect into account when taking a planar x-ray image. In *ImaSim*, the effect is only modeled along the cathode anode direction to speed up calculations, but the model is easily extended to the transverse direction.

To verify the results from *SpekCalc*, a MC simulation of an x-ray tube has been done using the BEAMnrc user code of the EGSnrc MC package. The x-ray tube consisted of a tungsten target with target angle θ. An electron beam with a 0.6 $\times$ 0.6 mm^2 square cross section was incident on the mid height point of the 5 cm high target. The field was collimated to 40 $\times$ 40 cm^2 at 100 cm source to detector distance (SSD) by a pair of lead jaws. The parameters ECUT and PCUT were set to 0.512 and 0.001 MeV respectively. Rayleigh scattering, bound Compton scattering, electron impact ionization and atomic relaxation were on. Directional bremsstrahlung splitting was also on with splitting number set to 500 and splitting radius 15 cm at 10 cm SSD. The number of simulated electrons was 4×10^8 and the phase space files were scored at 5 cm SSD. The number of particles in the phase space files varied with accelerating potential and tube angle: 1.4×10^6 for 90 kVp and $\theta = 5$ degrees to 5.4×10^6 for 140 kVp and $\theta = 25$ degrees. The beam was filtered by 1 mm Al and 0.11 mm Cu.

SpekCalc was used to calculate, using equation [3.6], photon spectra in a 2 $\times$ 2 cm^2 detector plane situated at a 5 cm SSD. The compared parameters are the two-dimensional total fluence map at the detector level as well as the mean energy map along the cathode-anode direction.

The shape of the fluence map is shown in Fig. 26 for a 120 kVp beam with 15 degree anode. The distribution is clearly influenced by the heel effect, which decreases the fluence towards the anode, and by the inverse square law. It is interesting to note that target attenuation has an effect in the transverse direction. Profiles of this beam, as well as an 80 kVp beam with 5 degree target angle and a 140 kVp beam with 25 degree target angle are shown in Fig. 27 to Fig. 29.

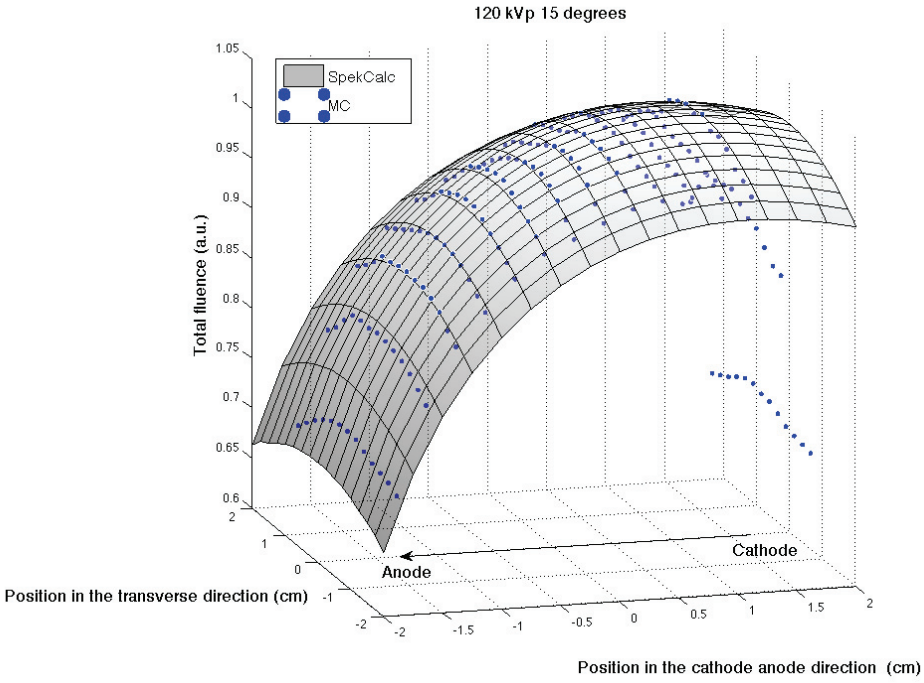

Figure 26: Comparison of two dimensional fluence maps at the detector level from a 15 degree anode and 120 kV accelerating potential. Both distributions are normalized to 1 at the central detector point. The decrease in fluence towards the anode is characteristic of the heel effect. The large discrepancy between MC (points) and *SpekCalc* (surface) towards the cathode is due to MC collimation which is absent in *SpekCalc*.

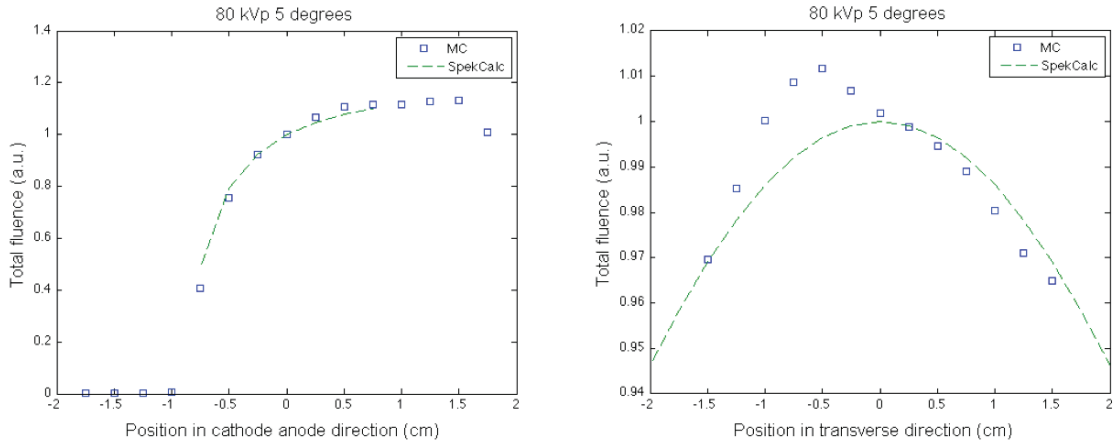

Figure 27: Comparison of MC and *SpekCalc* fluence map central profiles for an 80 kVp beam with 5 degrees target angle. Both distributions are normalized to 1 at the central detector point. The uncertainty in the cathode anode direction is contained in the data points and does not exceed 2%. In the transverse direction it varies between 0.5% and 0.7%.

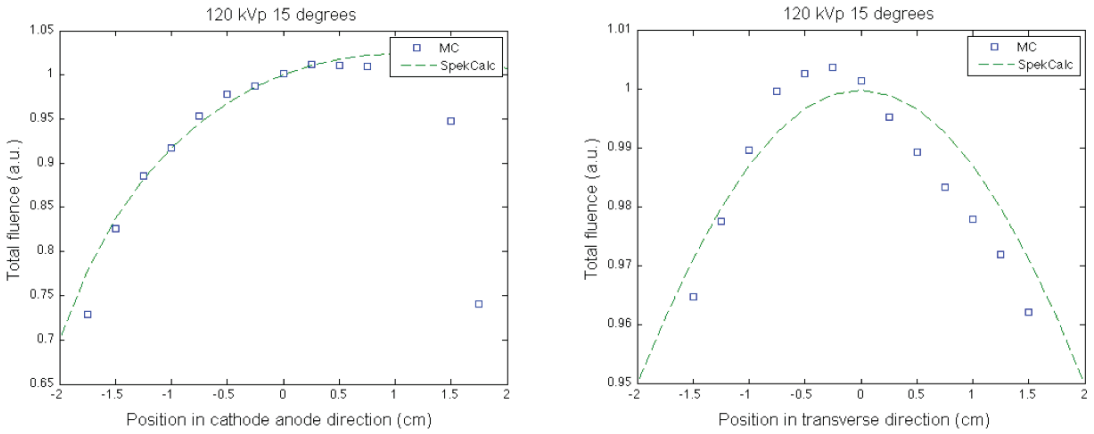

Figure 28: Comparison of MC and *SpekCalc* fluence map central profiles for a 120 kVp beam with 15 degrees target angle. Both distributions are normalized to 1 at the central detector point. The uncertainty in the cathode anode direction is contained in the data points and does not exceed 1%. In the transverse direction it varies between 0.4% and 0.5%.

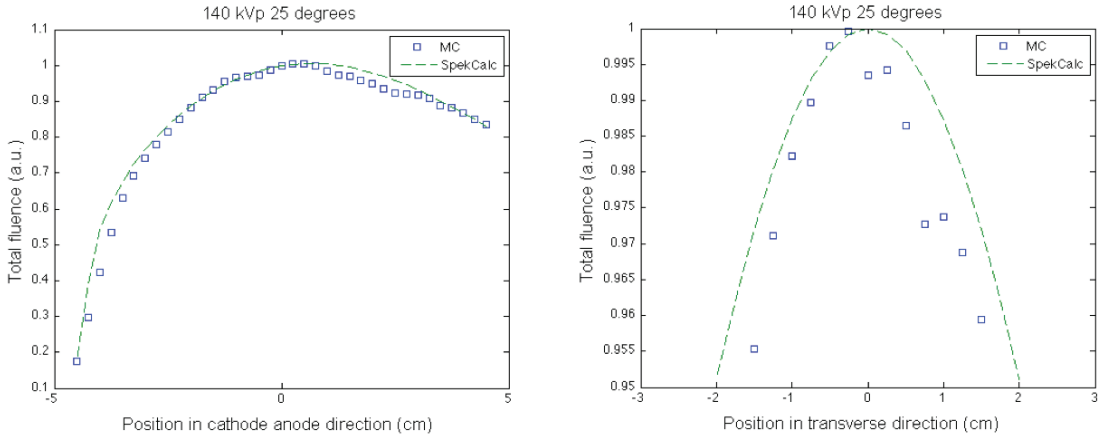

Figure 29: Comparison of MC and *SpekCalc* fluence map central profiles for a 140 kVp beam with 25 degrees target angle. Both distributions are normalized to 1 at the central detector point. The uncertainty in the cathode anode direction is contained in the data points and does not exceed 2%. In the transverse direction it varies between 0.5% and 1%.

The central beam profiles show good agreement in the cathode anode direction for the three beams. There are some major discrepancies for the 120 kVp beam, but they stem from the collimation present in the MC simulation. The

transverse profiles seem to agree less but the scale covers a 5 % variation in total fluence.

Fig. 30 shows the mean energy maps for the 140 kVp beam with 25 degree target and the 80 kVp beam with a 5 degree target. It shows that the mean energy increases towards the anode due to the increased target filtration which hardens the beam. The agreement for the lower energy and small angle is excellent, while at higher energy there seems to be a 2 keV discrepancy towards the cathode. In general, the analytical model of *SpekCalc* seems to model the heel effect sufficiently well for teaching purposes.

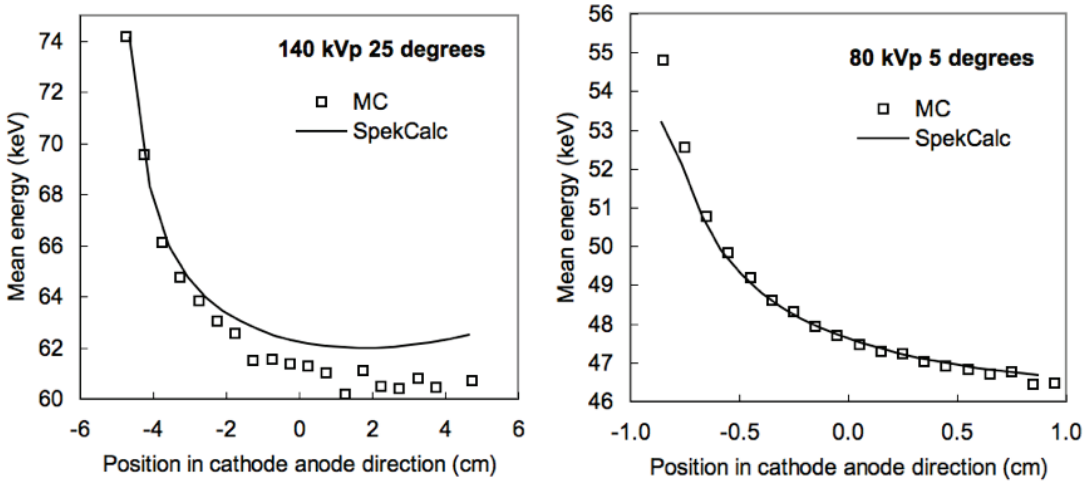

Figure 30: Comparison of mean energy maps along the cathode anode direction generated with *SpekCalc* and MC. The anode is at the left of the figures. The uncertainty is within 1 keV for both distributions.

4.3.1.3 Focal spot blurring

ImaSim provides the ability to simulate the effects of a finite focal spot. This is done by having multiple source points on the angled face of the target. The user needs to specify the electron beam size and the number of source points used and the simulation will transport photons from each of these points. A finite focal spot introduces geometrical blurring in the image. This is shown in Fig. 31 where an image taken with a 10×10 mm^2 beam sampled at 100 points is compared to a point source setup. The target is at 30 degrees and a 100 keV mono energetic beam has been used. A 10×10 mm^2 beam is unrealistic but was used to amplify the blurring effect. The blurring is clearly visible at the four

edges. It is more significant in the transverse direction (top and bottom) than the cathode anode direction (left to right). This is because the angled anode reduces the effective focal spot size only in the cathode anode direction. Furthermore, the blurring is more significant on the anode side since the effective focal spot size increases from left to right due to the target angle.

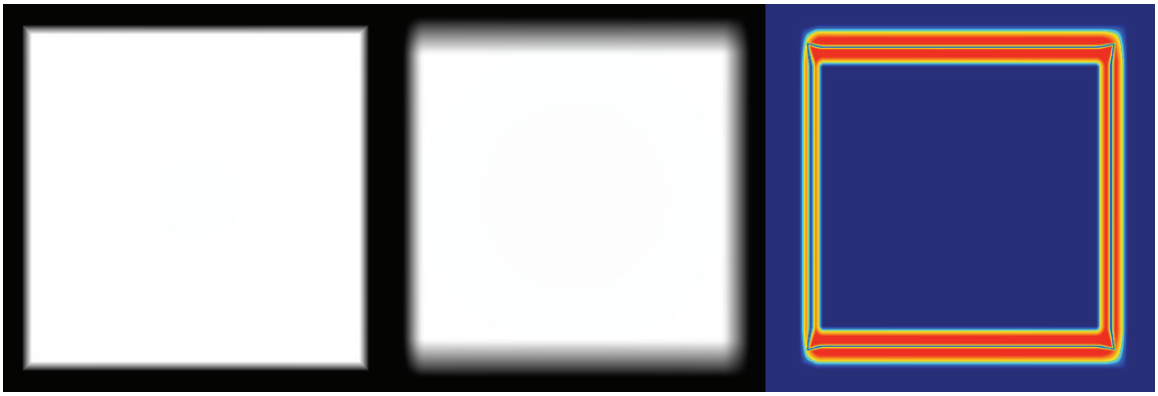

Figure 31: X ray images, with (middle) and without (left) blurring, of a $4 \times 4 \times 1$ cm^3 water slab whose bottom is positioned at 17 cm from the source and at 14 cm from the 10×10 cm^2 detector (0.2 mm/pixel). A gamma comparison with 1% of local value dose criterion and 0.5 mm DTA criterion has been used to highlight differences (right). Regions displayed with the yellow to red color scale fail the gamma test.

4.3.2 Portal imaging phenomena

The main difference between kV planar imaging and MV planar imaging is the beam's energy. At MV energies, the main interaction mechanism is the Compton effect, as explained in Section 2.2.4. The higher energy translates in a more penetrating beam. When comparing a kV image with an MV one, the contrast is reduced in the MV image. Fig. 32 shows that for a given material, different thicknesses will provide better contrast at kV energies than MV. The object imaged is the step wedge presented in Fig. 22. We see that the contrast between the thinnest and thickest part of the object is almost doubled with kV imaging compared to MV imaging. Another interesting aspect is the reduced beam hardening in MV imaging. We see in Fig. 32 that the contrast between successive steps is more constant in MV imaging than in kV imaging, where the beam gets harder with increased thickness, which causes contrast to decrease.

Fig. 33 shows profiles taken across an image of 4 slabs of muscle, water, adipose tissue and bone. We see that for MV and kV imaging, muscle and water are quite equivalent. In kV imaging, water, adipose tissue and bone have a good contrast difference because their effective Z is different (7.42, 5.92 and 13.8 respectively)[1]. This difference does not produce good contrast at MV energies due to the Compton effect dominance and only bone is discernable from soft tissues.

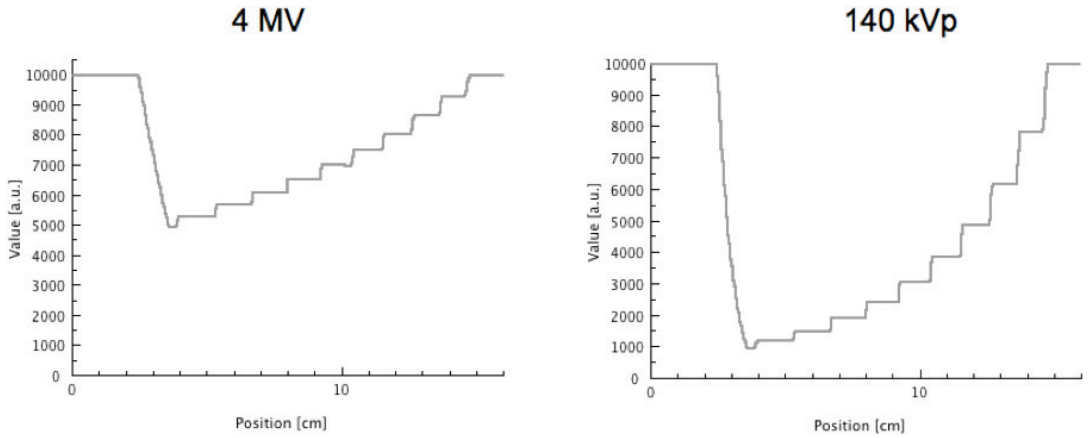

Figure 32: Contrast difference between an MV (left) and kV (right) simulation. We see that contrast is greater in kV imaging than MV. Contrast between successive steps decreases in kV imaging due to beam hardening, which is less important in MV imaging. Values have been normalized to 10 000.

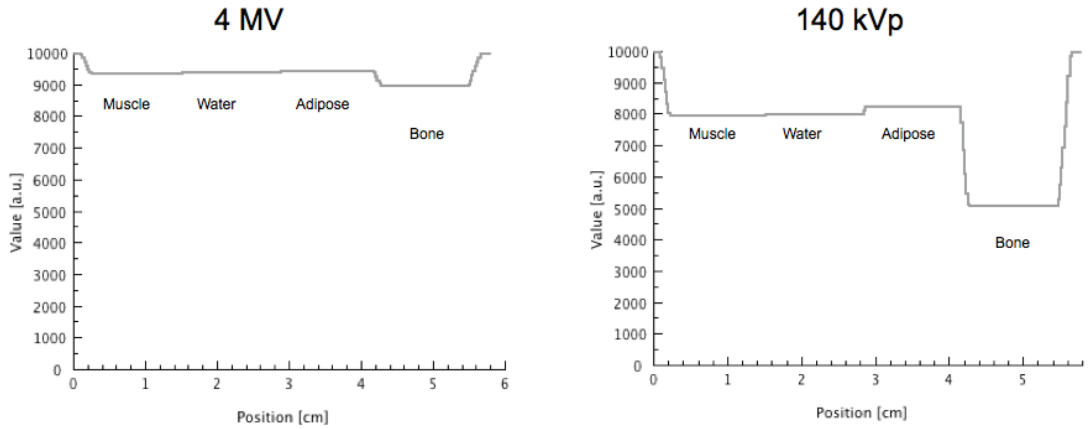

Figure 33: Contrast between tissues for MV and kV beams. We see that in MV imaging, tissues have similar attenuation and only bone is easily distinguished. Values have been normalized to 10 000.

4.3.3 CT imaging phenomena

4.3.3.1 Beam hardening artefacts

A. Cupping and correction

Beam hardening in CT causes a cupping artefact. Portions of the beam going through the central section of a uniform water cylinder are more hardened than those going through the sides. This means that the central portion of the image will have a lower attenuation values than the sides, resulting in a cupping artefact, as shown in Fig. 34.

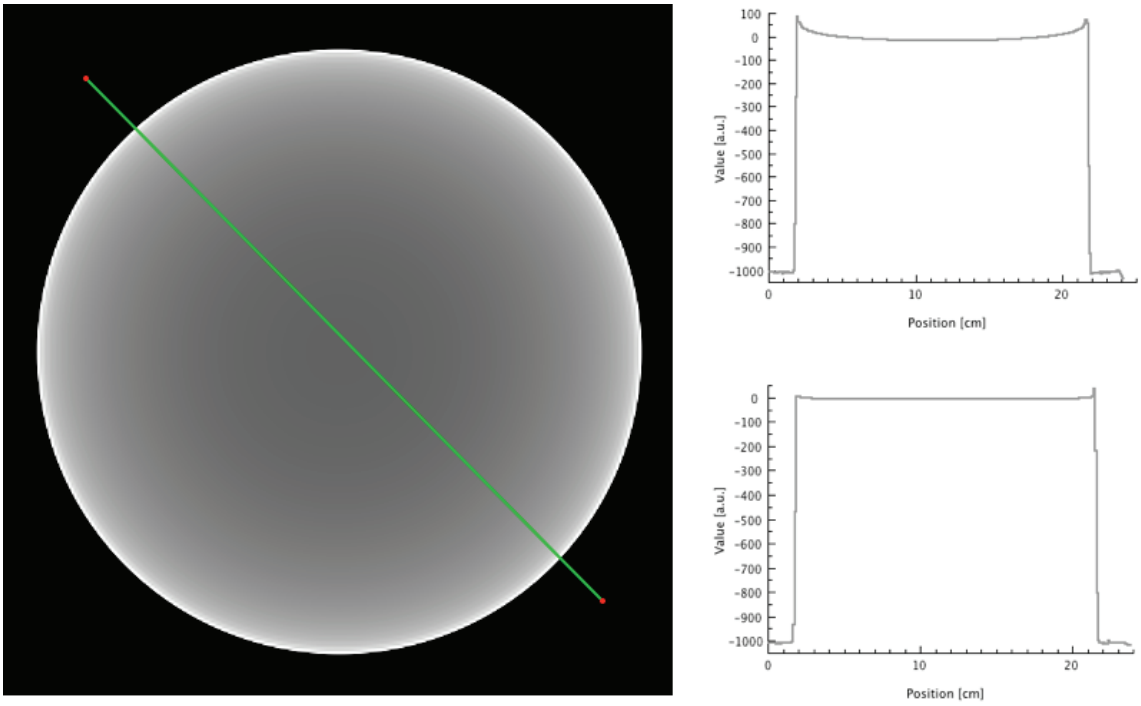

Figure 34: Cupping artefact in a CT image (left) of a uniform water cylinder with 10 cm radius. The beam used is 140 kVp with 5 mm Al filtration. The window width and level have been adjusted to highlight the cupping. The uncorrected profile (top right) illustrated the magnitude of the cupping artefact. The correction (bottom right) works well with this particular object. The values are HU.

The correction artefact presented in Section 3.9.1.6 corrects the effects for this particular geometry since it is based on a uniform water cylinder. Non cylindrical or non water objects would not be corrected as well.

B. Streaking

Another artefact stemming from beam hardening is the streaking artefact. This artefact consists of low HU values between objects with high attenuation such as bones or metal. These low HU values create dark streaks between the objects in question. Fig. 35 shows the artefact stemming from a 140 kVp beam. A similar image taken with a mono energetic beam does not show the artefact, indicating that spectral effects are responsible. At MV energies, the beam hardening from high Z materials is not as significant and the artefact is not visible.

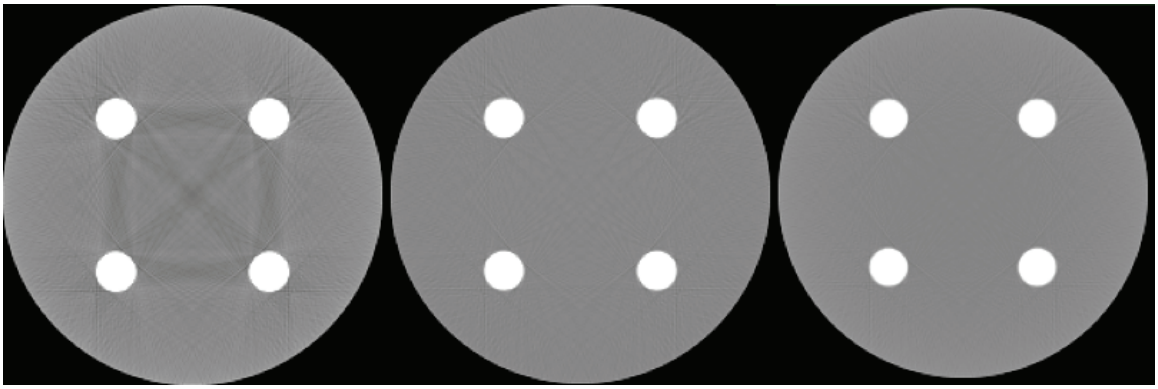

Figure 35: Streaking artefact due to beam hardening. An image taken with a 140 kVp beam (left) which is hardened shows the artefact. Images taken with a mono energetic 100 keV beam (middle) and a 4 MV beam (right) do not show the artefact since beam hardening is not present or minimal. The window width and level cover -500 to 500.

4.3.3.2 Effect of filters

Using the Shepp Logan or cosine bell filters introduce blurring in the reconstructed image since the high frequency content of the image is reduced. The cosine bell has the most important smoothing effect. This is shown in Fig. 36 where an image reconstructed with the Ram Lak filter is subtracted from an image reconstructed with the cosine bell filter. Since the cosine bell reconstructed image has more smoothing, there is a non-zero difference at the edges of sharp objects. The object used to create the images is the phantom presented in Section 4.2.2, with a 100 keV mono energetic beam and a 512 detector array.

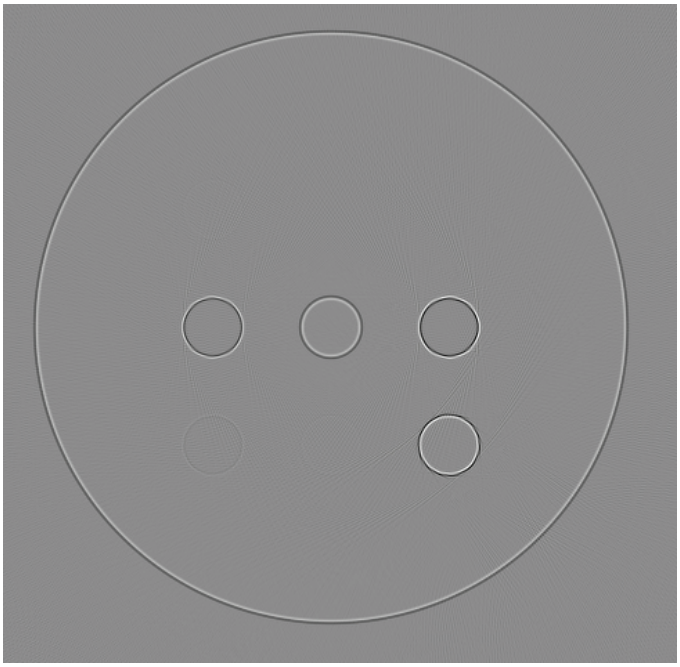

Figure 36: Difference image between a Ram Lak reconstructed image and a cosine bell reconstructed image. The black and white rings indicate that the cosine bell image is smoother.

4.3.3.3 Zero padding artefacts

Insufficient zero padding leads to dishing and DC artefacts, as explained in Section 3.9.1.3. These artefacts are shown in Fig. 37 as well as the effect of zero padding on their amplitude. We see that with no zero padding, reconstruction of a uniform water cylinder scanned with a 256 detector array yields a curved profile (dishing) as well as non zero HU values (DC). Increasing the zero pad order reduces the artefacts.

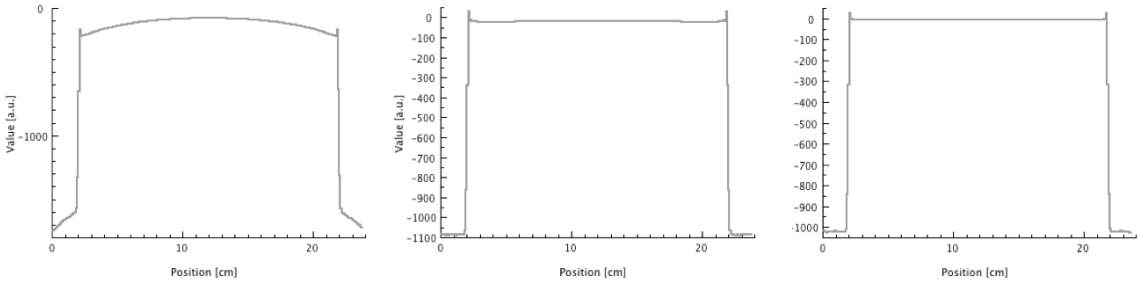

Figure 37: Effects of zero padding on the reconstruction. No zero padding (left) leads to severe dishing and DC artefacts. First order zero padding (middle) greatly reduces the artefacts and second order zero padding (right) eliminates them. The values are HU.

4.3.4 CBCT imaging phenomena

All imaging phenomena presented in the CT section are found in CBCT. The main difference of CBCT images with CT images is that they have a lower quality. There are at least two reasons for this. One is the absence of scatter rejection mechanism for flat panel detectors. In CT, individual detectors are collimated, which greatly reduces scatter. This phenomenon cannot be demonstrated with *ImaSim* since scatter is currently ignored. The other reason is that the FDK algorithm yields an approximation of the real image. Although correct in the central axial plane, images that are reconstructed further away from that plane suffer from a loss of quality. This can be shown with *ImaSim*. Fig. 38 shows the central axial image as well as an axial image taken at the edge of a cylindrical phantom. The geometry is the same as the example of Fig. 24. The scan has been done with a 100 keV mono energetic beam to reduce the effects of beam hardening and the object extends from –5 cm to +5 cm. The degraded quality of the non central axis image is clearly visible. The profile shows a kind of cupping artefact.

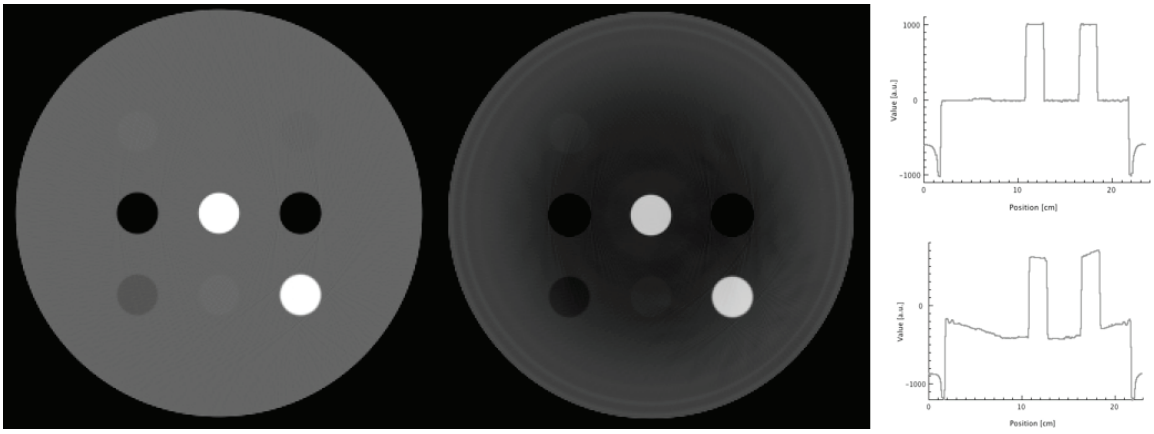

Figure 38: Lower quality of CBCT reconstruction in non central axial slices. Left is an axial image reconstructed at the central position. Center is an image of the same cylindrical object taken at 4.8 cm from the central position. Top right is a profile of the central slice while bottom right is a profile of the other slice. The image quality is clearly degraded. The values are HU.

REFERENCES

[1] T. S. Curry, J. E. Dowdey and R. C. Murry, *Christensen's Physics of Diagnostic Radiology*, 4th ed. (Lea & Febiger, Philadelphia, 1990).

CHAPTER 5: CONCLUSION

5.1 Summary

A software package containing a simulation environment for medical x-ray imaging, named *ImaSim*, has been created. With the aid of a simple yet attractive GUI, the user can virtually explore image creation with the main x-ray based imaging modalities found in a radiology or radiation oncology department. Not only can *ImaSim* provide a user with virtual medical images, but it enables him to modify a large array of parameters related to image formation and study their effect on the quality of the final image. The production of x-rays, the effects of diverse objects and materials, geometrical setup, detector response and data processing can all be studied. Some technical phenomena such as the heel effect or CT artefacts can be simulated at the click of a button to provide the user with insight.

ImaSim has the potential to reduce the need for hands on experiment with expensive and heavily used equipment. Furthermore it eliminates the risk of damaging medical equipment and provides the user with a liberty over imaging parameters not found in an imaging suite. Simulations can be easily managed in a classroom setting by an educator or in a self learning setting by a student.

The use of a validated x-ray source model, *SpekCalc*, provides *ImaSim* with a solid physical foundation. Modifications to the model, validated by MC experiments, provide a complete, two dimensional description of the x-ray beam. The addition of accurate cross section data from the XCOM and MC generated detector response curves help to make *ImaSim* simulations as exact as possible. The ray tracing algorithm ensures that calculation times remain reasonable.

With built in image analysis tools, *ImaSim* is a complete, standalone package which can simplify the teaching of medical x-ray imaging and enhance the learning experience

5.2 Future Work

The exactness of simulations in *ImaSim* would be improved by the modelling of scattered radiation. A modification of the ray tracing algorithm would then be required, either by a MC treatment or by using pencil beam scatter kernels [1]. Including scatter in simulations would yield more realistic images, especially for CBCT. The treatment of scatter would also make the study of scatter rejection methods such as grids or air gaps possible.

The reduction of calculation times, which can be long for CBCT calculations, would be necessary if scatter was to be modelled. Various avenues could be explored, such as more efficient coding, the use of a faster programming language or graphical processor unit (GPU) implementation. GPU implementation has been recently shown to dramatically decrease calculation times in some ray tracing applications[2].

A faster code would also enable calculation in voxel geometries, which is more time consuming. This would open the door to the utilisation of real patient data from clinical scans as object and provide a more realistic simulation.

Finally, other photon based imaging modalities could be added to *ImaSim*. Positron emission tomography (PET) would be an ideal candidate since it is based on the emission of two opposed gamma rays. A user would simply need to specify volumes containing isotopes which would then act as photon sources. The detector geometry would be very similar to the already present CT geometry.

REFERENCES

[1] W. J. C. Elmpt, S. Nijsten, B. J. Mijnheer and A. W. H. Minken, "Experimental verification of a portal dose prediction model," Medical Physics **32**, 2805-2818 (2005).

[2] S. Hissoiny, B. Ozell, P. Després, "Fast convolution-superposition dose calculation on graphics hardware," Medical Physics **36**, 1998-2005 (2009).

APPENDIX A

The mathematical relationship between the thickness $s(x,\theta,\vec{r})$ of target material filtering the emitted photon spectra and the emission depth x, target angle θ and detector position $\vec{r}$ and will be shown. The reader is referred to Fig. 8, chapter 3. The emission depth l will be replaced by x. The detector position $\vec{r}$ will be specified by the angle α in the anode cathode direction and by the position y in the transverse direction. Using the law of cosines, the emission point to detector distance L is given by:

$$L = \left[x^2 + \frac{d^2}{\cos^2\alpha} - 2x\frac{d}{\cos\alpha}\cos\left(\frac{\pi}{2}+\alpha\right)\right]^{1/2} \qquad [4.1]$$

where

$$\alpha = \arctan\left(\frac{x}{d}\right). \qquad [4.2]$$

Using the law of cosines again, the angle φ is given by:

$$\varphi = \arccos\left(\frac{L^2 + \frac{d^2}{\cos^2\alpha} - x^2}{2L\frac{d}{\cos\alpha}}\right) \qquad [4.3]$$

and angle ψ is given by:

$$\psi = \arcsin\left(\frac{d}{L}\right). \qquad [4.4]$$

Using the law of sines, the distance H between the focal spot point F and the attenuated emission point E_a is given by:

$$H = \frac{d}{\cos\alpha}\frac{\sin\varphi}{\sin(\pi-\varphi-\alpha-\theta)}. \qquad [4.5]$$

Making use of the law of sines again gives:

$$s(x,\theta,\vec{r}) = H\frac{\sin\left(\frac{\pi}{2}-\theta\right)}{\sin(\psi)}. \qquad [4.6]$$

If the detector point is at a distance y from the anode cathode axis (it would be pointing out of the page in Fig. 8) at point D_y then angle β is $\angle DED_y$. This angle is given by:

$$\beta = \arctan\left(\frac{y}{L}\right) \qquad [4.7]$$

and the new distance $s'(x,\theta,\vec{r})$ is:

$$s'(x,\theta,\vec{r}) = \frac{s(x,\theta,\vec{r})}{\cos\beta}. \qquad [4.8]$$

APPENDIX B

The HVL is the thickness $t_{1/2}$ of a given material required to halve the intensity of a pencil beam of x-rays. For a mono energetic beam, the following equation is valid:

$$\frac{1}{2} = \frac{I}{I_0} = e^{-\mu \cdot t_{1/2}} \rightarrow t_{1/2} = \frac{\ln 2}{\mu}. \qquad [5.1]$$

When measuring the HVL of a poly energetic beam, one generally uses an ionisation chamber. The signal given by such a chamber is not energy independent, since the energy absorption coefficient μ_{en} varies with energy. The signal will be dependent on the energy deposited in the air volume:

$$I \propto \int_0^{E_{\max}} N(E) E \mu_{\text{en}}^{\text{air}}(E) dE. \qquad [5.2]$$

It is the intensity from equation [5.2] that needs to be halved to obtain the HVL. This approach is taken in *ImaSim* when HVLs from the spectra generated by *SpekCalc* need to be calculated.

BIBLIOGRAPHY

L. E. Antonuk, "Electronic portal imaging devices: a review and historical perspective of contemporary technologies and research," Physics in Medecine and Biology **47**, R31-R65 (2002).

T. M. Buzug, *Computed Tomography*. (Springer, Berlin, 2008).

T. S. Curry, J. E. Dowdey and R. C. Murry, *Christensen's Physics of Diagnostic Radiology*, 4th ed. (Lea & Febiger, Philadelphia, 1990).

J. V. Dyk, "The Modern Technology of Radiation Oncology," (Medical Physics Publishing, Madison, 1998).

W. J. C. Elmpt, S. Nijsten, B. J. Mijnheer and A. W. H. Minken, "Experimental verification of a portal dose prediction model," Medical Physics **32**, 2805-2818 (2005).

L. A. Feldkamp, L. C. Davis and J. W. Kress, "Practical cone-beam algorithm," Journal of the Optical Society of America A **1**, 612-619 (1984).

S. Hissoiny, B. Ozell and P. Després, "Fast convolution-superposition dose calculation on graphics hardware," Medical Physics **36**, 1998-2005 (2009).

M. Hoheisel, "Review of medical imaging with emphasis on X-ray detectors," Nuclear Instruments and Methods in Physics Research A **563**, 215-224 (2006).

A. C. Kak and M. Slaney, *Principles of Computerized Tomographic Imaging*. (Society of Industrial and Applied Mathematics, 2001).

D. A. Low, W. B. Harms, S. Mutic and J. A. Purdy, "A technique for the quantitative evaluation of dose distributions," Medical Physics **25**, 656-661 (1998).

R. Mohan, C. Chui and L. Lidofsky, "Energy and angular distributions of photons from medical linear accelerators," Medical Physics **12**, 592-597 (1985).

J. P. Moy, "Recent developments in X-ray imaging detectors," Nuclear Instruments and Methods in Physics Research A **442**, 26-37 (2000).

X. Pan, "Optimal noise control in and fast reconstruction of fan-beam computed tomography image," Medical Physics **26**, 689-697 (1999).

E. B. Podgorsak, *Radiation Physics for Medical Physicists*. (Springer, Berlin, 2006).

G. Poludniowski, G. Landry, F. DeBlois and F. Verhaegen, "SpekCalc X-ray Spectrum Generator Programme," (The Institute of Cancer Research, 2008).

G. Poludniowski and P. Evans, "Calculation of x-ray spectra emerging from an x-ray tube. Part I. Electron penetration characteristics in x-ray targets," Medical Physics **34**, 2164-2174 (2007).

G. Poludniowski, "Calculation of x-ray spectra emerging from an x-ray tube. Part II. X-ray production and filtration in x-ray targets," Medical Physics **34**, 2175-2186 (2007).

W. H. Press, S. A. Teukolsky, W. T. Vetterling and B. P. Flannery, *Numerical Recipes in C*. (Cambridge University Press, Cambridge, 1992).

D. W. O. Rogers, B. A. Faddegon, G. X. Ding, C. Ma and J. We, "BEAM: A Monte Carlo code to simulate radiotherapy treatment units," Medical Physics **22**, 503-524 (1995)

M. Stock, B. Kroupa and D. Georg, "Interpretation and evaluation of the γ index and the γ index angle for the verification of IMRT hybrid plans," Physics in Medecine and Biology **50**, 399-411 (2005).

S. Webb, *The Physics of Medical Imaging*. (Institute of Physics Publishing, Bristol, 1988).